Institute for Ship Structural
Design and Analysis (M-10)

Project Thesis

Examination of the stress concentration factor of single and multiple ellipsoidal defects by means of finite element method

(Untersuchung von Spannungskonzentrationsfaktors einzelner und mehrfacher
ellipsoider Defekte mit Hilfe der Finite-Elemente-Methode)

Author: Abdullah Younes

Matriculation number: 21380758

Institute: Institute for Ship Structural Design and Analysis (M-10)

First Supervisor: Prof. DSc. (Tech.) Sören Ehlers

Second Supervisor: M.Sc. Moritz Braun

Datum: 25.02.2021

Statutory Declaration

„I, Abdullah Younes, declare that I have composed this thesis myself and without the use of any other than the cited sources. Sentences or parts of sentences quoted literally are marked as such; other references with regard to the statement and scope are indicated by full details of the publications concerned. The thesis in the same or similar form has not been presented to any examination body and has not been published. This thesis was not yet, even in part, used in another examination or as a course performance. “

Place, date

Signature

Acknowledgements

First and foremost, I would like to thank M.Sc. Moritz Braun for discussing several topics with me at the beginning. He helped a lot during the process of learning the commands of ANSYS APDL. Furthermore, he gave useful advice on how to continue the work during the ongoing pandemic.

Special thanks goes to M.Sc. Hauke Herrnring for taking his time and helping me with the installation of the license server on my personal computer.

Last but not least, I would like to thank my my mother, Zakia Younes and my father, Mohammad Rahim Younes for their permanent support, motivation and patience during this work.

TUHH
Technische Universität Hamburg

Konstruktion
und Festigkeit
von Schiffen

TUHH · M-10 · Am Schwarzenberg Campus 4C · D-21073 Hamburg

PROJECT THESIS 2021

for

Abdullah Younes

Examination of the stress concentration factor of single and multiple ellipsoidal defects by means of finite element method (Untersuchung von Spannungskonzentrationsfaktors einzelner und mehrfacher ellipsoider Defekte mit Hilfe der Finite-Elemente-Methode)

Defects are known to be one of the main causes of failure in powder bed fusion based additively manufactured components. Especially, the interaction of multiple defects can reduce fatigue strength significantly.

Hence, this project deals with the determination of stress concentration factors at single and multiple ellipsoidal defects. For this purpose, two- and three-dimensional finite element models shall be created to determine stress concentration factors at such defects. The project contains the following tasks:

1) Development of parametric finite element models of components containing ellipsoidal defects
2) Determination of stress and stress concentration factors for various configurations including single and multiple defects of different sizes and distances from free surfaces as well as different orientation between multiple defects
3) The results shall be compared with literature references

Literature studies of specific topics relevant to the thesis work shall be included.

The work scope may prove to be larger than initially anticipated. Subject to approval from the supervisors, topics may be deleted from the list above or reduced in extent.

In the thesis the candidate shall present his personal contribution to the resolution of problems within the scope of the thesis work.

Theories and conclusions should be based on mathematical derivations and/or logic reasoning identifying the various steps in the deduction.

The candidate should utilise the existing possibilities for obtaining relevant literature.

Thesis format

The thesis should be organised in a rational manner to give a clear exposition of results, assessments, and conclusions. The text should be brief and to the point, with a clear language and the objective to be published in a conference article and/or scientific journal. It is thus desirable that the thesis is written in English. Telegraphic language should be avoided.

The thesis shall contain the following elements: An executive summary, list of symbols and acronyms, followed by the main body of the thesis consisting of a brief background introduction, a state of the art defining the knowledge gaps defining the scope or work and limitations, the actual contribution chapters, conclusions with recommendations for further work, references and (optional) appendices. All figures, tables and equations shall be numerated.

The supervisors require that the candidate, in an early stage of the work, presents a written plan for the completion of the work. The plan may include a budget for the use of computer and laboratory resources if applicable, which will be charged to the department. Overruns shall be reported to the supervisors.

The original contribution of the candidate and material taken from other sources shall be clearly defined following basic academic principles and an acknowledged referencing system, which includes the name of the referred authors followed by the publication year in the text. The subsequent reference list can thus be alphabetical.

The report shall be submitted in two copies:

- Signed by the candidate
- The text defining the scope included
- In bound volume(s)
- Drawings and/or computer prints, which cannot be bound should be organised in a separate folder.
- The report shall also be submitted in PDF along with essential input files for computer analysis, spread sheets, MATLAB files etc. in digital format.

Ownership

According to the current rules, the candidate has the ownership of the thesis. Any use of the thesis has to be approved by TUHH M-10 (or external partner when this applies). TUHH M-10 has the right to use the thesis as if a TUHH M-10 employee carried out the work, if nothing else has been agreed in advance.

Thesis supervisors

Prof. Sören Ehlers, Moritz Braun

Deadline: 25.02.2021

Hamburg, 25.08.2020

Table of Content

List of Abbreviations

2D	2-dimensional
3D	3-dimensional
AM	Additive Manufacturing
CAD	Computer aided Design
HIP	Hot Isostatic Pressing
SLM	Selective Laser Melting

List of Figures

List of Symbols

Symbol	Unit	Description
A_0	mm^2	Unloaded cross section area
a_{El}	mm	Ellipse axis perpendicular with load direction
a_{cir}	mm	Circular void radius
A_T	mm^2	Total area
A_V	mm^2	Void area
b_{El}	mm	Ellipse axis in line with load direction
D_{cyl}	mm	Cylinder diameter
d_{sph}	mm	Spherical void diameter
d_v	mm	Void diameter
e	mm	Eccentricity
E	N/ mm^2	Young`s modulus
F	N	Applied Force
H_{cyl}	mm	Cylinder height
K_t	-	Stress concentration factor
l_0	mm	Original specimen length
L_e	mm	Edge length of 2D plane
l_n	mm	New specimen length
r	mm	Radial coordinate of Polar coordinate system
R_{cyl}	mm	Cylinder radius
$R_{p0,2}$	N/mm^2	Yield strength
s_v	mm	Void distance
V_T	mm^3	Total Volume
V_V	mm^3	Void Volume

Δl	mm	Length difference
ε	-	Strain
ε_x	-	Strain in X-direction
ε_y	-	Strain in Y-direction
ε_z	-	Strain in Z-direction
θ	-	Angle coordinate in polar coordinate system
ν	-	Poisson’s ratio
σ	N/ mm^2	Applied stress
σ_{max}	N/ mm^2	Maximum stress
$\sigma_{max,El}$	N/ mm^2	Maximum stress of ellipse
σ_{nom}	N/ mm^2	Nominal stress
σ_r	N/ mm^2	Radial stress in polar coordinates
σ_x	N/ mm^2	Stress in X-direction
σ_y	N/ mm^2	Stress in Y-direction
σ_z	N/ mm^2	Stress in Z-direction
σ_θ	N/ mm^2	Circumferential stress in polar coordinates
$\sigma_{\theta,max}$	N/ mm^2	Maximum circumferential stress
$\tau_{r\theta}$	N/ mm^2	Shear stress in polar
Φ_{Ar}	-	Areal porosity
Φ_{Vol}	-	Volumetric porosity

List of Tables

1 Introduction

The appearance of porous structures in natural objects such as rocks and stones are very common. The porosity is often created during the fabrication of the object. The lack of material inside an object leads to a significant downfall of the strength and density [Davis et al., 2017].

Nowadays, even in modern fabricating processes such as the additive manufacturing (AM) pores exist inside the produced parts. AM is a technique which creates 3-dimensional (3D) parts layer-by-layer directly from a 3D computer aided design (CAD) file. Various of different AM methods exists depending on the laser source, material used or procedure. Highly complex parts can be manufactured and be directly used in various applications in the aerospace, automotive and biomedical industry, which are impossible to create with conventional manufacturing techniques [Yadollahi and Shamsaei, 2017].

Especially manufacturing parts with the selective laser melting (SLM) method, where metallic powder is used, causes porosity in the final product. The porosity has a negative influence on several material properties such as the Young’s modulus [Choren et al., 2013] and fatigue resistance [Garb et al., 2018]. In addition, porous shapes inside a part can also cause intensely high local stress values [Schnabel et al., 2019]. This and other microstructural impurities are the reason why an uncertainty exist among the mechanical properties of SLM parts [Yadollahi and Shamsaei, 2017]. In order to realize the full potential of SLM, these irregularities must be researched thoroughly.

The finite element method (FEM) is a very common computational method to examine structures under load. Approximate solutions are given to practical problems in the real world. In the last decades, the improving computer performance played a significant role in the rise of FEM, due to the computation of the partial differential equations. An FEM analysis is nowadays necessary for structures or parts applied in various fields of engineering. FEM is an excellent alternative when the experiment is costly and time consuming [Khairallah et al., 2016].

In this work, the focus will be to analyze circular and spherical voids inside basic 2-dimensional (2D) and 3D structures in regard to the high local stress, respectively. The simulations will be performed with the help of the FEM software ANSYS Mechanical APDL. Particularly, the size and position of the pores will be varied and evaluated.

AM parts are being tested currently by Institute for Ship Structural Design and Analysis at the technical university of Hamburg on the mechanical properties. Figure 1-1 shows additive manufactured specimen that are being used for tensile, fatigue and bending test.

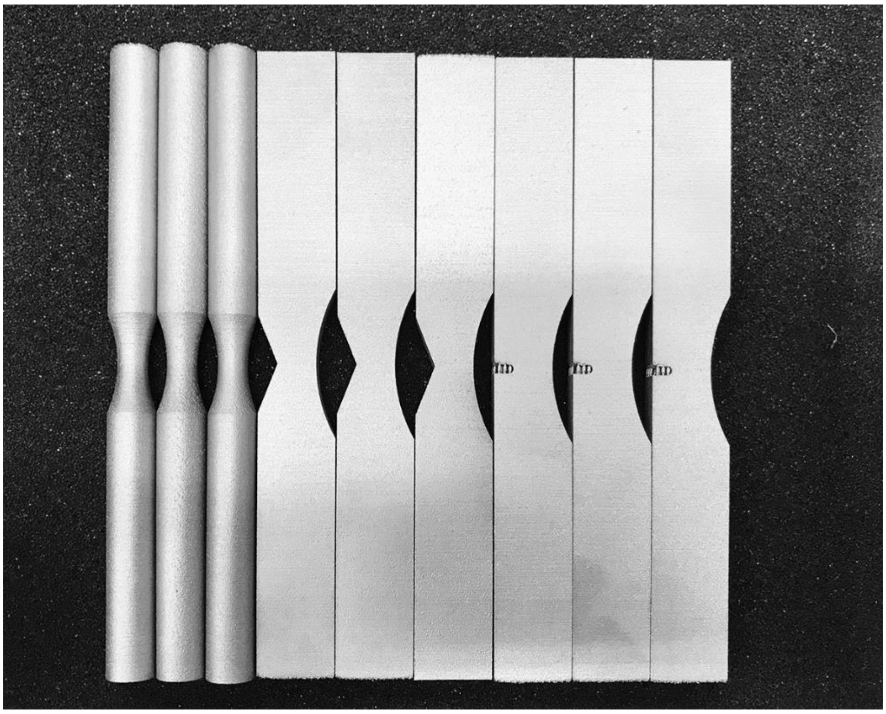

Figure 1-1: Specimen for tensile and bending testing fabricated by SLM [Braun et al., 2020]

2 Theory

2.1 Additive manufacturing

Additive manufacturing (AM) is a revolutionary technology, where 3D parts are built by adding successive layers of material [Celik, 2020]. Different materials such as metals, polymers and ceramics can be used to create objects. Highly complex lightweight structures can be fabricated if the 3D-CAD part exist. Furthermore, with AM a high level of product customization can be achieved due to the degrees of freedom. According to the Wohler report, the annual money spent worldwide on final part production by AM in 2019 almost reached 1.5 billion US-Dollars [Wohlers Associates]. Figure 2-1 shows a clear rising tendency in money spent each year since 2007.

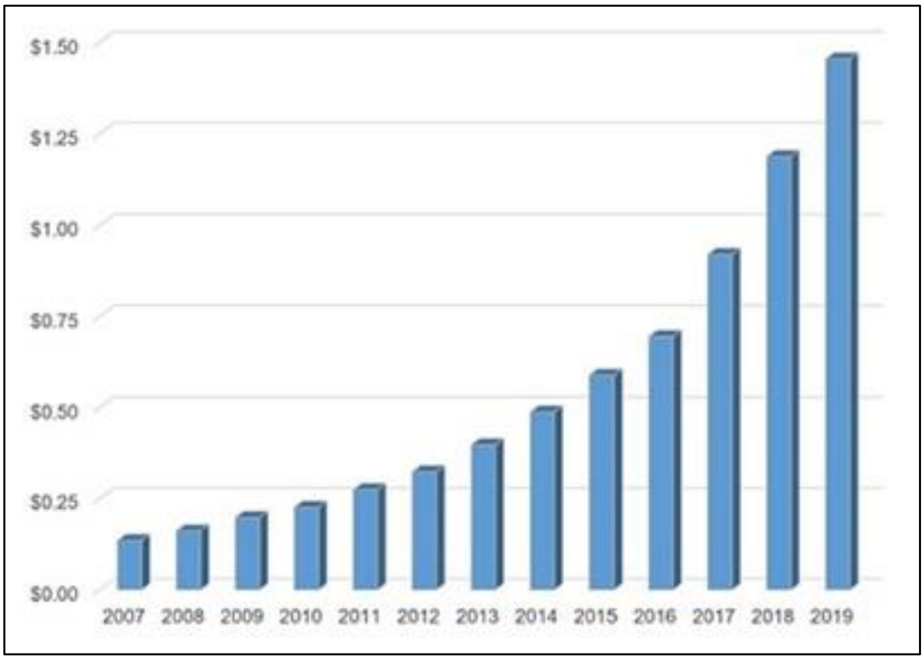

Figure 2-1: Money spent annually on AM products worldwide in billions of dollars [Wohlers Associates]

Many different types of AM procedures exist. It is possible to divide AM procedures into different categories depending on the process, the material and energy source. However, according to the DIN EN ISO/ASTM 52900 (2018) AM has been classified into seven groups. In Table 1 an overview of the different categories and the associated methods and materials is listed [Celik, 2020].

Table 1: AM categories

AM category	AM methods	Material
Vat Photopolymerization	Stereolithography, Digital light Processing, Continuous liquid interface production	Polymers (Epoxides)
Material jetting	Polyjet printing, Multijet printing	Polymers
Binder jetting	Binder jetting	Starch, Metals, Ceramics
Powder bed fusion	Selective laser sintering Selective laser melting	Thermoplastics, Metals (Steel), Ceramics
Material extrusion	Fused filament fabrication, Direct write, Liquid deposition modeling	Thermoplastic, polymers
Directed energy deposition	Directed energy deposition	Metals
Sheet lamination	Sheet lamination	PVC, Paper, Sheet metals

The application of AM takes place in various fields as can be seen in figure 2-2. This illustrates the importance of AM parts nowadays.

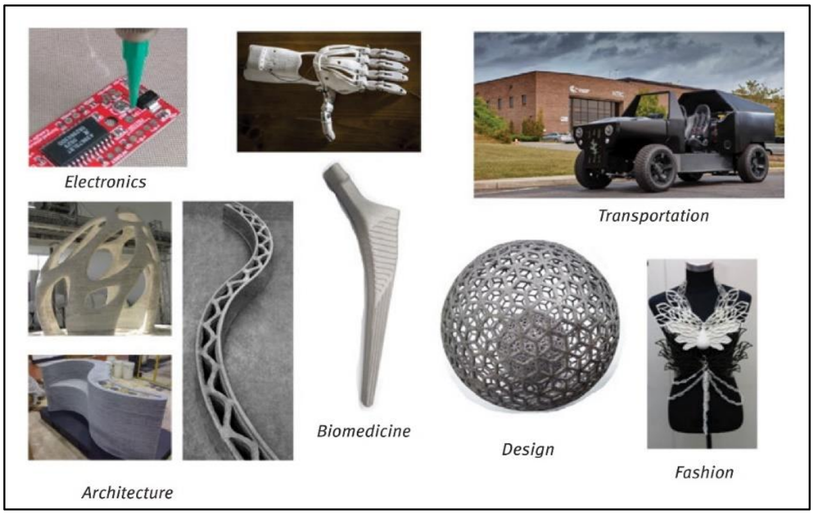

Figure 2-2: Various applications of additive manufacturing [Celik, 2020]

2.2 SLM procedure

SLM belongs to the layer-by-layer powder-bed variants of the AM techniques. It was developed by the Fraunhofer Institute ILT in 1994 [Prashant, 2014]. SLM provides the best mechanical properties out of all AM procedures involving metals [Celik, 2020]. Figure 2-3 shows the SLM 280 machine manufactured by the company SLM Solutions [SLM-SOLU].

Figure 2-3: Selective Laser Melting 280 (SLM 280) machine [SLM-SOLU]

The first steps of the whole procedure take place in the computer. A 3D-CAD model that represents the geometry of the desired part needs to be generated [Prasanth, 2014]. On top of that, the support structure must be modeled as well, if necessary. Usually when parts have an overhang that is not supported by any layers below, an appropriate support structure is needed. Since the SLM machine requires a layer-by-layer information of the end product, the part needs to be "sliced" into layers in CAD [Prashanth, 2014]. This step is also called 2D-Slicing. Lastly the CAD-file needs to be exported into a STL-file, which is a universal format for CAD-data, since every software has its own format.

As shown in the simplified model in figure 2-4, the typical SLM machine components inside the chamber are a building platform, a powder delivery platform, a recoater blade, a laser beam and a moving mirror. First, the recoater blade transfers metallic powder from the delivery platform onto the building platform [Klocke, 2015]. On the way back, the blade distributes the metallic powder evenly on the surface by removing the excessive powder to make the surface as level as possible. Thereafter, the laser will fully melt the powder with the help of a moving mirror, directing the coordinates [Klocke, 2015]. The powder particles will absorb the energy from the laser beam and heat up above the melting point. In a liquid state the particles will fuse together and solidify quickly, since the entire process the chamber is filled with Argon gas.

Argon gas is used in the SLM machine chamber as a measure against the creation of impurities since Argon is inert [SLM-SOLU]. It will not allow the atmosphere to react with the process in any way or form due to the chemical inactivity. Furthermore, the constant gas flow can successfully lead the smoke, that is created due to overheating the powder, away.

Already, the first layer which will be the bottom layer of the end product, has been established. The delivery platform will now raise while the building platform will sink by the amount of a layer thickness. Again, the blade will transport the powder into the building platform and the laser can melt the next layer. During the melting of the current layer, the previous layer, which is underneath the current one will also melt because of the strong laser energy. This allows a fuse together of consecutive layers. This procedure repeats itself until the top and final layer has been created [Klocke, 2015]. The gas of the chamber will be removed via the gas outlet. After removing the metallic powder surrounding the produced part can be extracted from the SLM machine. Produced parts that contain support structure, needs to be removed as well.

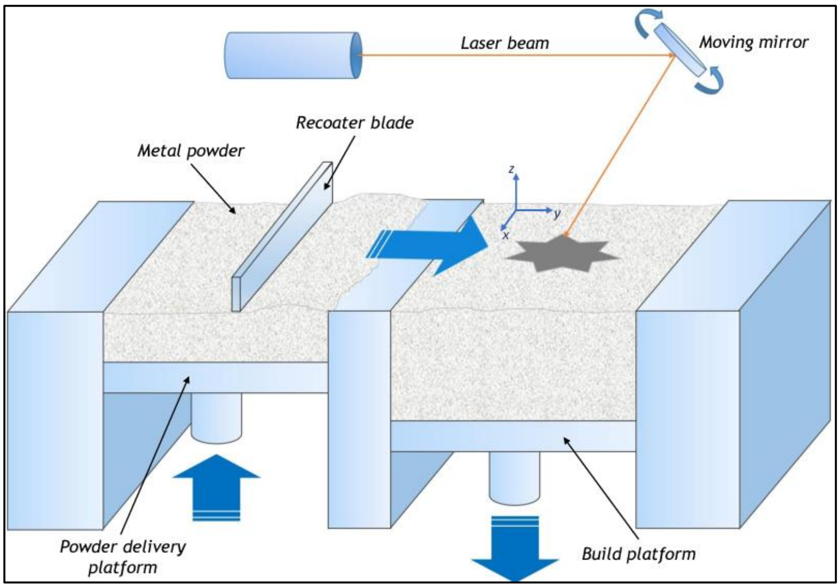

Figure 2-4: SLM function principle [Griffiths et al., 2019]

2.3 Porous structures

During the AM fabrication process, the creation of irregularities inside the printed part can occur. Depending on the process parameters such as laser power, scanning velocity and layer thickness etc. following undesirable effects can occur: unmolten powder particles, entrapped gas bubbles, cracks and other types of irregularity [Kasperovich et al., 2016]. The entrapped gas during melting leads to spherical-shaped pores whereas unmolten regions lead to irregularly shaped voids [Yadollahi and Shamsaei, 2017].

To characterize the graduality of a porous structure, the porosity parameter Φ is introduced. It describes the relation between the void volume (addition of all porous volumes) and the total volume [Garb et al., 2018].

$$\Phi_{Vol} = \frac{V_V}{V_T} \tag{1}$$

For 2D structures following formula can be derived:

$$\Phi_{Ar} = \frac{A_V}{A_T} \tag{2}$$

The range for the porosity parameter amounts from zero to one, where zero is a complete nonporous body and one is a fully porous body (not practical).

The total porosity can vary extremely, and it is very difficult to measure. Moussaoui et al. (2018) measured a porosity between 0,45% and 1,38% with scanning electron microscopy from 35 cubes made of Inconel 718 with a dimension of 20mm x 20mm x 20mm after the SLM process. Tillmann et al. (2016) measured the largest pore radius to be 26,8µm and the smallest to be 2,13µm from SLM produced rectangles made from Inconel 718 with a dimension of 27mm x 7mm x 1,5mm with light microscopy. Although the shape, the size and the quantity of pores are all important factors that weigh in on the strength properties of the material, it is the location of the pores inside a part is particularly critical according to Yadollahi and Shamsaei (2017). It is suggested that pores near the surfaces are more likely to cause cracks. Figure 2-5 shows the result of a Computer Tomography scan of a SLM part [Braun et al., 2020]. Pores of different sizes in the micrometer range can be seen on the surface of the part. The figure proves that pores are an important feature of SLM parts.

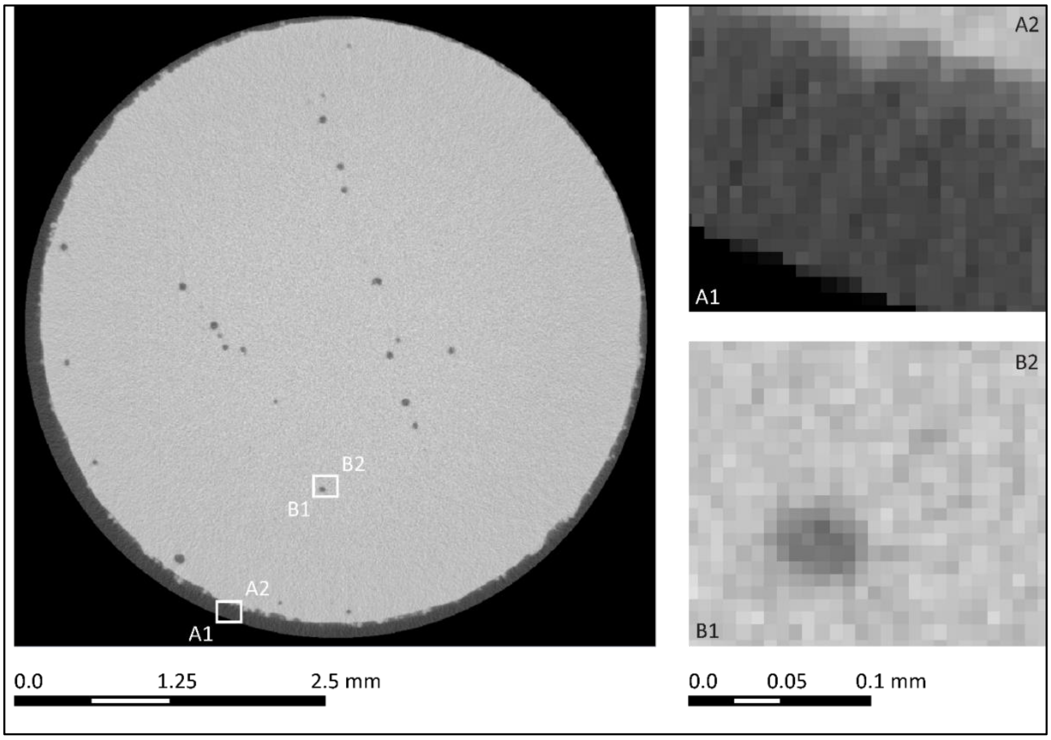

Figure 2-5: CT-Scan of SLM part showing pores [Braun et al., 2020]

A measure to reduce the existing pores after the SLM process is to use hot isostatic pressing (HIP). The additive manufactured part is exposed to very high temperatures and pressure over a period of time. The total porosity was reduced significantly after HIP as a post-treatment following the SLM process [Moussaoui et al., 2018; Tillmann et al., 2016]. However, not all pores can be eliminated. Especially the pores near the surface remain, while internal pores are reduced.

2.4 Tensile stress

In structure mechanics, there are many kinds of material failures occurring. Under static load, materials begin to deform with increasing tensile force applied. The stress σ is defined as the the uniaxial force *F* divided by the cross-section area A_0 [Bürgel, 2005]. In the example of a tensile test, the force applied will lead to a contraction of the cross-section area. The index *0* hence refers to the unloaded cross section area, which is constant.

$$\sigma = \frac{F}{A_0} \tag{3}$$

In the case of metals, the strain ε is linear proportional with the stress *σ*. The slope of the linear rise is also known as the Young`s Modulus *E* [Bürgel, 2005]. This relation is called the elastic region or Hooke’s law and it is fully reversible once the load is removed.

$$\sigma = E * \varepsilon \tag{4}$$

With the strain *ε* defined as the elongation Δl divided by the original or unloaded length of the specimen l_0.

$$\varepsilon = \frac{\Delta l}{l_0} = \frac{l_n - l_0}{l_0} \tag{5}$$

The Young’s Modulus is a very important material property, and it is a measure for the strength of the bonds between atoms and molecules, which can also be related to the melting point. Materials with higher melting point tends to possess a high Young’s modulus as well and vice versa [Bürgel, 2005]. Although the stress is uniaxial ($\sigma_x \neq 0$, $\sigma_y = 0$, $\sigma_z = 0$), it does cause a strain in in all three coordinates (X, Y and Z) of the cartesian coordinates system. While the strain in X-direction remain positive, the strains in the other directions are negative. A linear relation exists between the strains [Bürgel, 2005]:

$$\varepsilon_y = \varepsilon_z = -\nu * \varepsilon_x = -\nu * \frac{\sigma_x}{E} \tag{6}$$

The constant *ν* is called Poisson`s ratio and is material dependent.

The elastic region ends with the yield strength $R_{P0,2}$. Beyond the yield stress is the beginning of the plastic deformation. The plastic region is non-linear and irreversible, and it allows large strains of a material before the breaking or fracture point, as can be illustrated in Figure 2-6. Materials with such behaviour are called ductile. However, not all metals have the ability of a large plastic deformation. These metals are likely to fracture or break completely shortly after the applied stress exceeds the yield strength. Materials without or with very small plastic deformity are called brittle. The exact transition between the elastic and plastic region is very difficult to measure and varies from material to material. Therefore, the yield strength is determined whenever 0,2% plastic deformation has occurred [Bürgel, 2005].

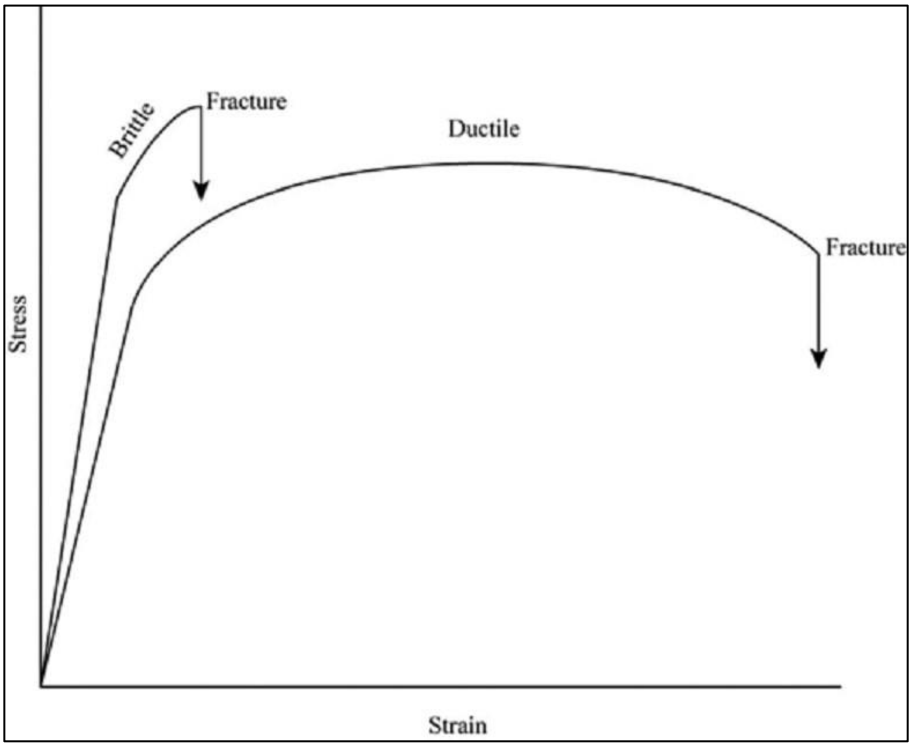

Figure 2-6: Stress-strain diagram for a brittle and ductile material [Info-Palace]

The following table shows the values of the Young's modulus, Poisson´s ratio and Yield strength for the super alloy Inconel 718 at room temperature [MAHER].

Table 2: Material properties of Inconel 718

Material	Youngs`s Modul *E*	Yield Strength $R_{p0,2}$	Poisson`s ratio
Inconel 718	200 GPa	1034 MPa	0,294

Inconel 718 mainly consists of Nickel, Aluminum and Chromium. It has excellent strength and corrosion properties, even at high temperatures [Moussaoui et al., 2018], which makes it suitable for various applications in the fields of aeronautical and automotive engineering, where the operating temperatures are high. Due to the hardness, it is difficult to manufacture with conventional methods such as machining due to the wear of the cutting tools [Moussaoui et al., 2018]. In addition, the low thermal conductivity of Inconel 718 leads to high temperatures during machining [Costes et al., 2006]. SLM offers a new opportunity for manufacturing Inconel 718, where the powder particles are processed [Tillmann et al., 2016].

2.5 Stress concentration

In this section the stress theory behind having a hole inside mechanical geometries under tensile load is described analytically. Initially a 2-dimensional plane part with an elliptical void will be analyzed first followed by a 3D cylinder elliptical void.

Geometrical impurities in a body, such as holes or notches, can disrupt the uniform stress distribution across the entire body [Dieters and Bacon, 1988]. In the regions near the irregularity the stress value is much higher than the average stress values far away from the irregularity.

A way to understand the stress concentration is to look at the force lines under uniaxial stress [Fracturemechanics]. Figure 2-7 illustrates the path of these lines through a body with a circular hole. The lines would have been uniform if the hole had not been there. The presence of the hole forces the lines to move around the it, which results in the lines being very dense in certain parts around the hole. Dense lines are always a hint of high stress areas.

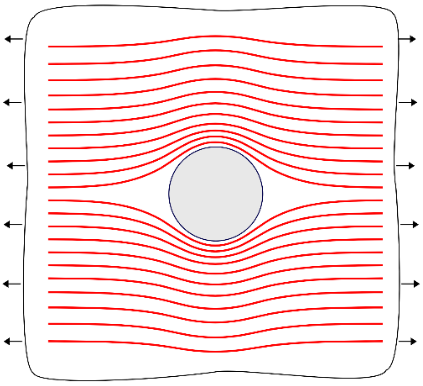

Figure 2-7: Force lines of an infinite plane with a circular hole [Fracturemechanics]

Furthermore, the force lines visually explain why sharp passages or notches, where the radius is rather small are causing high stresses. An abrupt change of the geometry squeezes many straight force lines tight together in a relatively small area. In contrast, smooth and round transitions with large radiuses force the lines together as well, but not that tightly and the increased stress distribution takes place over a larger area. The idea of force lines also exists in 3D bodies.

Figure 2-8 illustrates a 2-dimensional infinite long and wide plane with such an irregularity [W. Pilkey and D. Pilkey, 2008]. The hole or the void in the middle of the rectangular shaped plane induces a stress concentration in certain parts of the plane. Without the hole, the stress would be uniformly distributed, and it would be equal to the load applied divided by the cross-section. Not only does the void function as a stress raiser when it is axially loaded, it also creates a localized zone of biaxial stress [Dieters and Bacon, 1988]. Since the plane is infinite, the increased and decreased stress values of the local zone fade to uniform stress distant from the void.

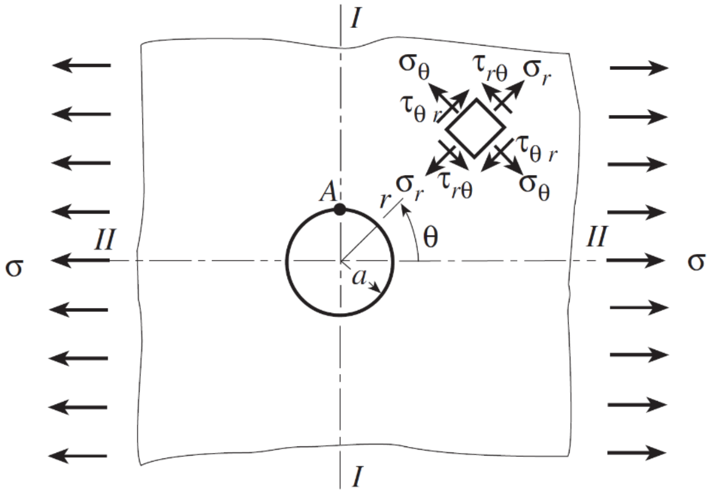

Figure 2-8: Infinite plane with circular hole [W. Pilkey and D. Pilkey, 2008]

Because of this reason, the stress concentration factor K_t is introduced, which is the maximum stress divided by the nominal stress. The nominal stress is usually selected in an area where the stress concentration has no influence, which is typically far away [Dieters and Bacon, 1988].

$$K_t = \frac{\sigma_{Max}}{\sigma_{Nom}} \tag{7}$$

This particular problem has already been solved analytically [Timoshenko, 1970]. By using polar coordinates and assuming the length and width of the plate are infinite, the stresses can be expressed as:

$$\sigma_r = \frac{\sigma}{2}\left(1 - \frac{a^2}{r^2}\right) + \frac{\sigma}{2}\left(1 + 3\frac{a^4}{r^4} - 4\frac{a^2}{r^2}\right)\cos(2\theta) \tag{8}$$

$$\sigma_\theta = \frac{\sigma}{2}\left(1 + \frac{a^2}{r^2}\right) - \frac{\sigma}{2}\left(1 + 3\frac{a^4}{r^4}\right)\cos(2\theta) \tag{9}$$

$$\tau_{r\theta} = -\frac{\sigma}{2}\left(1 - \frac{a^2}{r^2}\right) + \frac{\sigma}{2}\left(1 + 3\frac{a^4}{r^4} - 4\frac{a^2}{r^2}\right)\cos(2\theta) \tag{10}$$

With *r* being the radial and *θ* being the angular coordinate of the polar coordinate system. The starting point for *r* is the center point of the hole. The angular coordinate *θ* starts at the 3 o'clock position and moves counterclockwise as in figure 2-8. Furthermore, σ is the applied stress and a is the radius of the hole, as displayed in figure 2-8. In order to calculate the stresses around the edge of the hole, the radial polar coordinate r is set to the value of the hole radius a. The formulas above simplify and result in [W. Pilkey and D. Pilkey, 2008]:

$$\sigma_r\ (r = a) = 0 \tag{8}$$

$$\sigma_\theta\ (r = a) = \sigma\ [1 - 2 * cos(2\theta)] \tag{9}$$

$$\tau_{r\theta} = 0 \tag{10}$$

The stress in angular coordinate, also called circumferential stress, is varied from 0° to 360° from the formula and the solution is plotted in figure 2-9. The applied stress was set to 1 N/mm^2 as an example. For this case, the stress around the void coincides with stress concentration around the void.

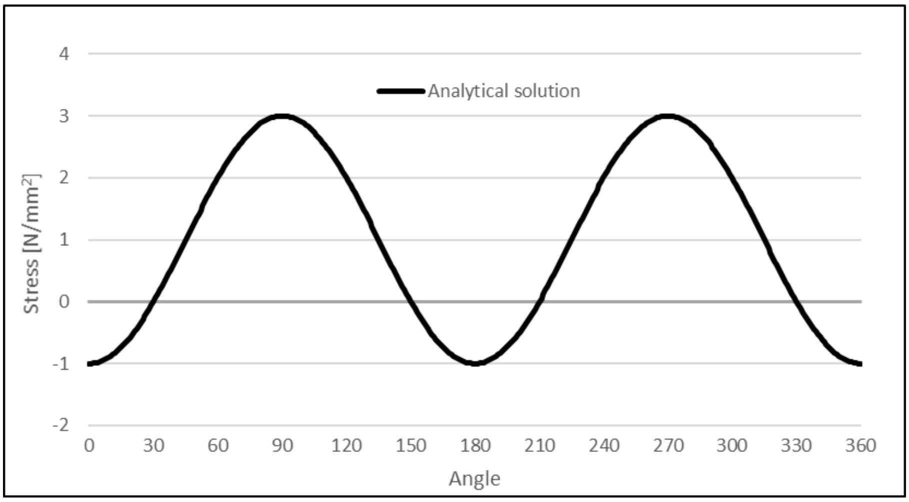

Figure 2-9: Analytical circumferential stress around the void

The outcome of this formula is symmetric and periodic. The maximum stress is located at 90° degrees and at the diametrical opposite point 270° degrees with a value of 3 N/mm^2 or 3σ, which leads to a stress concentration factor of 3. At 0° degrees and 180° degrees the resulting stress is at negative σ. At 30° degrees and 210° degrees the stress vanishes.

For a finite 2D plane with edge length L_e, the void diameter d_v has been varied. A formula from Heywood (1952) has been updated for the stress concentration factor by W. Pilkey and D. Pilkey (2008):

$$K_t = \frac{2+(1-d/L_e)^3}{1-(d/L_e)} \tag{13}$$

The formula has been plotted in the figure 2-10.

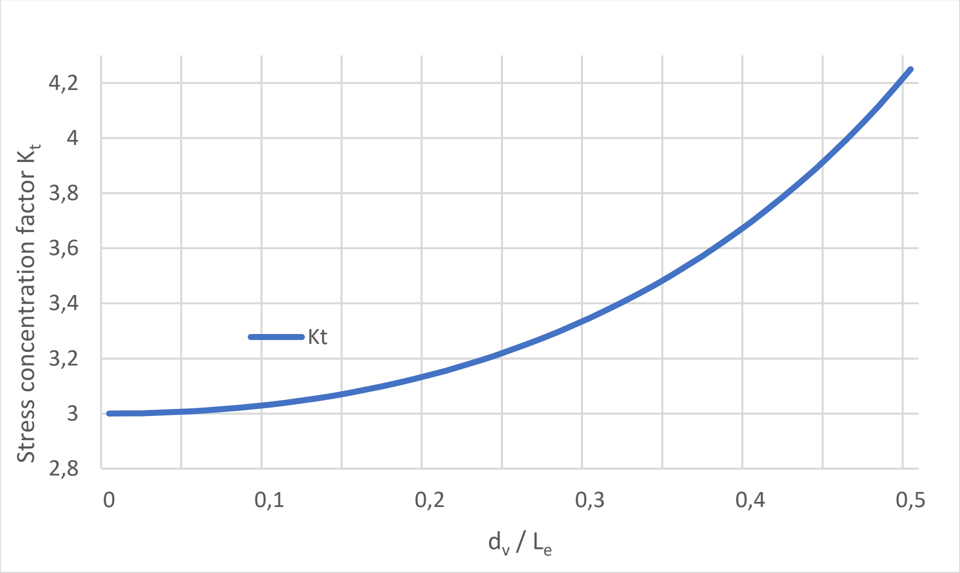

Figure 2-10: Stress concentration factor of plane with varied void sizes

Only the ratio range between 0 and 0,5 is of importance. Above 0,5 the stress does not result in uniform stress far away from the void. Hence, the stress concentration factor can not be calculated.

An elliptical hole under uniaxial tension in an infinite wide plane also functions as a stress raiser as shown in figure 2-11.

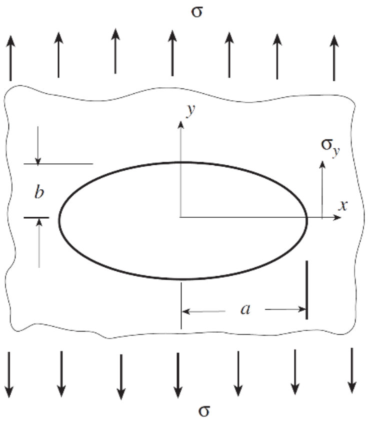

Figure 2-11: Plane with an elliptical hole under uniaxial stress [W. Pilkey and D. Pilkey, 2008]

The analytical solution for this problem is known. The maximum stress can be described with following equation [W. Pilkey and D. Pilkey, 2008]:

$$\sigma_{max,El} = \sigma * (1 + 2 * \frac{a_{El}}{b_{El}}) \qquad (12)$$

With a_{El} being the axis perpendicular and b_{El} being the axis in line with the tensile load. In this figure, a is the major and b is the minor axis. The maximum stress is proportional with the term a_{El}/b_{El}. So, for a very narrow hole, for example a crack, with $a_{El} >> b_{El}$, the resulting stress concentration will be very high. In the case of a circular hole ($a_{El} = b_{El}$), the equation will result in the equation above.

It is very important to examine the stress concentration factors for cavities in evaluating the effects of porosity materials [Peterson, 1965]. An infinite circular cylinder with a central spherical cavity Timoschenko (1970) exhibits a stress concentration factor of 2,045. For a finite cylinder with equally large height H_{cyl} and diameter D_{cyl} and with a central spherical void of diameter d_{sph}, the stress concentration factor has been calculated. The following diagram (fig. 2.12) has been reconstructed from W. Pilkey and D. Pilkey (2008) and depicts the stress concentration over the ratio between cavity diameter and cylinder diameter. Above the ratio of 0,45 the stress does not stabilize into a uniform stress value and is therefore represented by a dotted line.

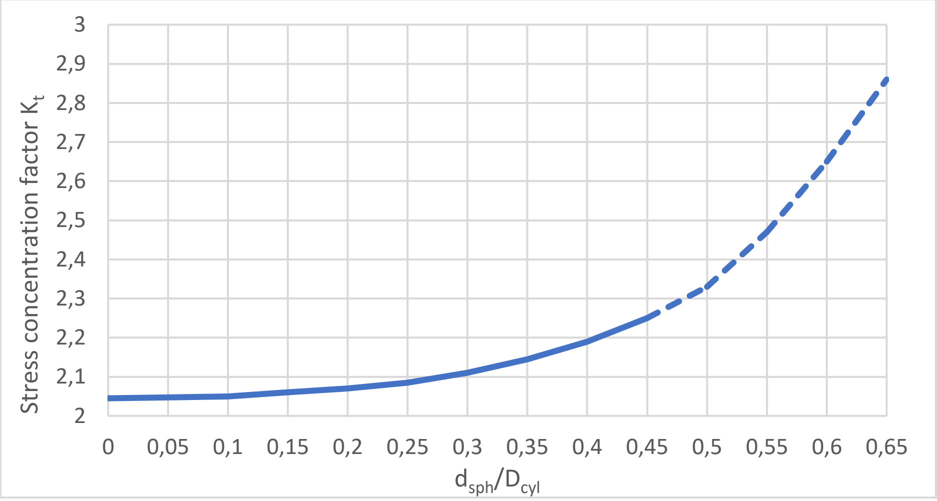

Figure 2-12: Stress concentration factor of cylinder with varied cavity sizes

A high stress concentration factor can be dangerous for both brittle materials and ductile materials. When the stress passes the yield stress under static load case, brittle materials will fracture completely, while with ductile materials a local plastic deformation takes place [Dieters and Bacon, 1988]. However, under dynamic load stress raisers initiate cracks inside a ductile material and ultimately reduce the fatigue strength [Tillmann, 2016].

2.6 Finite element method

The main principal of an FEM is to represent a large model by a finite number of elements which are connected to each other at their nodes [Madenci and Guven, 2015]. Numerous types of elements exist, but simple elements require less computational effort and are favored. The common elements such as the basic triangular element can cover any shape of a 2D body [Dieters and Bacon, 1988]. The number of nodes on a element can differ. Using more nodes increases the degree of freedom on an element, gives a better model representation and the final results will be more precise. However, the computational time and effort will increase as well [M. Thompson and J. Thompson, 2017].

Today, there are many software’s available for computing FEM analyses. In this work ANSYS mechanical APDL has been used. All FEM simulations in this work are based on loads with constant values over time, also called static loading. The procedure of a computational FEM can be divided in three major categories [M. Thompson and J. Thompson, 2017].

- *Preprocessor*: The solid model geometry is discretized. An element type is then being chosen for this specific problem. Suitable material properties are defined. The geometry needs to be meshed in full extent.

- *Solution*: The boundary conditions are defined. This is done by selecting nodes and setting the displacements to a specific value. The loading is applied by using single, pressure or volume loads. By solving, the algebraic equations are solved where the nodal displacements are the unknowns.

- *Postprocessor*: Results are plotted, viewed and exported. From the calculation of the nodal displacements, other results such as stress, strain and mode shapes can be derived.

The ability to analyze the loading on complex structures or structures with complex loading are the main advantages of the FEM analysis. Nevertheless, the element type and number of elements used determine the accuracy of the result. Also, the experience of the user plays a great factor regarding the accuracy of the result. Using insufficient boundary conditions or a wrongfully interpretation of the load will lead to errors in the analysis. The FEM software itself contains assumptions or ideal simplifications such as smooth surface geometries and the use of point loads just to name a few, which are not realistic in real life.

3 Simulation setup

3.1 Geometry

In the 2D analytical solution from chapter 2.4, infinite edge length of the plane was considered, which cannot be achieved with the simulation software. However, choosing edge lengths large enough in relation to void size, will lead to similar results. Therefore, a standard edge size of a 100mm x 100mm square will be selected for all 2D simulations. Only the circular void size, the number of voids and their position will be varied. In order to achieve this specific geometry, a quadratic area and a circular area will be defined. With the help of the Boolean operator “subtract” the circular area will be subtracted from the quadratic area and the void will be created.

The outer body for the 3D body is a cylinder with a radius of 50mm and a height of 100mm. The void will have a fully spherical shape and the radius will be varied as well. Again, the command Boolean “subtract” will be used.

Furthermore, for one simulation only one specific element type will be used, there will not be any mix of element types. The element size, however, can differ in a single simulation. Areas with special interest will be represented by more elements than other. Only structural elements, where the degrees of freedom are the displacements, will be used.

3.2 Meshing

A perfect mesh does not exist for analyzing a single object. There will always be different ways to mesh one object. In this work, not only different type of element will be used, but also the number of elements will be varied and subsequently compared in order to verify the results.

For the computation of the 2D-simulation the element “*PLANE183*”, an 8-noded quadrilateral or six-noded triangular, is used. A great advantage of the element is, that besides the corner nodes, there are also nodes between the corner points, which gives a single element more degrees of freedom and allows various shape deformations. The element “SOLID187”, a 3D 10-noded tetrahedron, will be used to discretize the cylinder.

Once the element is selected, material parameter such as the Young`s Modulus and the Poisson ratio of INC-718 are defined. In addition, isotropic material behaviour is presumed.

When the geometry has many irregularities, it will be difficult to use the “mapped mesh” throughout the simulations. Mapped mesh uses divisions, patterns and it requires many restrictions. The geometry ha to be designed in a way that supports the use of map meshing. The element size can be varied along the lines, which allows a dense mesh at certain areas of choice. On the contrary, smartsize meshing is very easy to define. The elements become denser towards the void.

3.3 Loading and boundary conditions

It is assumed that all loads will be applied infinitively slow, so a static case can be approached, and inertia forces can be neglected. In order to achieve perfectly uniaxial tension in plane direction across the body, it is sufficient to define the load on one side perpendicular to the surface and clamp the opposite side as in figure 3.1a, since the stress field will be equivalent. The displacements of the all the nodes on the left edge side (fig. 3-1a) are set to zero in X-direction. In addition, the node on the left bottom corner has no displacement in Y-direction. The loading is defined on the right edge side as a tensile surface load working on lines with a value of 20 N/mm^2.

Figure 3.1b shows the cylinder will be loaded on the top area with a tensile surface load of 20 N/mm^2 working on areas. On the bottom surface, all displacement values of the nodes will be set to zero so that the cylinder is fixed.

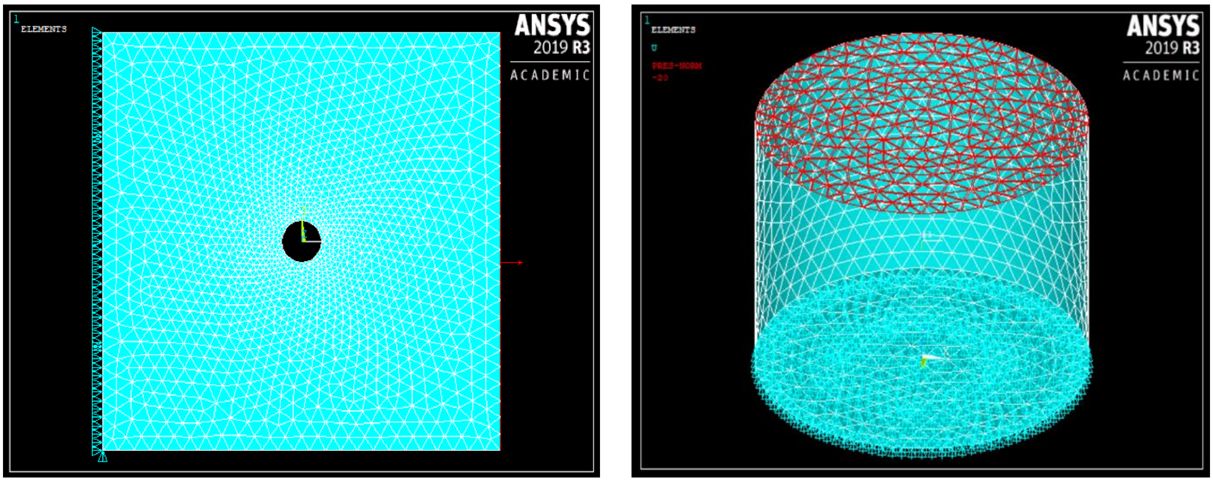

Figure 3-1: Loading and bearing of a) a 2D plane and b) a 3D cylinder

3.4 Finite element analysis with ANSYS Mech APDL

An example of a simulation of a 2D-plane with a central hole meshed by using smartsize mesh will be explained. It is loaded with 20 N/mm^2 on the right side and is fixed on the left side. The exclamation mark is the start of a comment. The commands and explanation are the following:

```
/CLEAR                        ! Deletes all previous commands
/PREP7                        ! Introduction to the preprocessor

ET,1,PLANE183                 ! Selecting PLANE183 elements
MP,EX,1,200000                ! Defines the Young`s Modulus
MP,PRXY,1,0.294               ! Defines the Poisson’s Ratio
RECTNG,-50,50,-50,50,         ! Creates a rectangle with corner points from -50 to 50 in X and Y coordinates
CYL4,0,0,5                    ! Creates a circle at the origin with a radius of 5
ASBA,    1,    2              ! subtracts Area 2 from area 1
SMRT,1                        ! Element size determined by smartsize level 1
AMESH,ALL                     ! Mesh all areas
!EREFINE,ALL,,,1              ! Level 1 refinement of all elements
SFL,2,PRES,-20,               ! Surface load on line 2 in form of pressure with a value -20
DL,4,,UX,0                    ! Displacement value of 0 in X-direction on the entire line 4
DK,1,UY,0                     ! Displacement value 0 on the keypoint 4 in Y-direction

/SOLU                         ! Entering the solution processor
SOLVE                         ! Solving the problem

/POST1                        ! Entering the Postprocessor
/EDGE,1,1,45                  ! Displays only the common lines
/GLINE,1,0                    ! Specifies the element outline style
RSYS,1                        ! Changes the coordinate system to cylinder coordinate system
/DSCALE,ALL,1                 ! Sets the displacement scale to 1.0
```

It has to be noted that after entering these commands, the option “Results Viewer” is chosen manually from user interface menu. The different kind of stress results can be easily displayed in the “Results Viewer”.

4 Results and Discussion

4.1 2D - Smartsize meshing

By using smartsize meshing with triangular elements on the 2D single void problem, elements get smaller and denser from the boundaries towards to void. The stress field looks symmetric on the first sight, however there are slight deviations when comparing the node values and locations. The origin is located in the center of the void. The circumferential stress is measured along the angular coordinate in a polar coordinate system, similarly to the analytical solution from chapter 2.4. In the case of figures 4-1, the void has a radius of 5mm. The stress scale at the bottom reveals, that the maximum and minimum stress value are 60,66 N/mm^2 and 20,4 N/mm^2 respectively, for this particular problem.

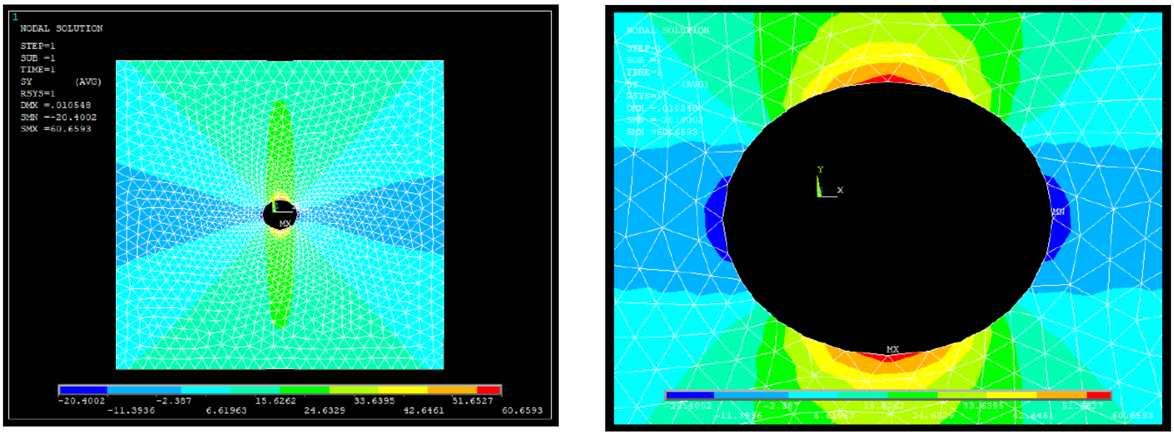

Figure 4-1: Triangular smartsize mesh of 2D plane with 5mm void. a) Complete structure b) zoom of void

The stress concentration factor can be calculated by dividing the maximum stress that exists by the nominal stress, which in this case can be assumed to be equal to the applied stress.

$$K_{t,\theta} = \frac{\sigma_{\theta,max}}{\sigma_{Nom}} = \frac{60{,}66\,\frac{N}{mm^2}}{20\,\frac{N}{mm^2}} = 3{,}03 \qquad (13)$$

Because the stress values vary greatly around the void, the nodal stress values have been plotted over the angular polar coordinate θ in figure 4-2. The graph shows a periodic behaviour with one period being 180 degrees. The antipodal points of the circular void possess the almost identical stress values. At 90° and 270° degrees the maximum stresses occur, while the minimum stress is located 0° (or 360°) and 180° degrees. At 30°, 150°, 210° and 330° the circumferential stress value reaches zero.

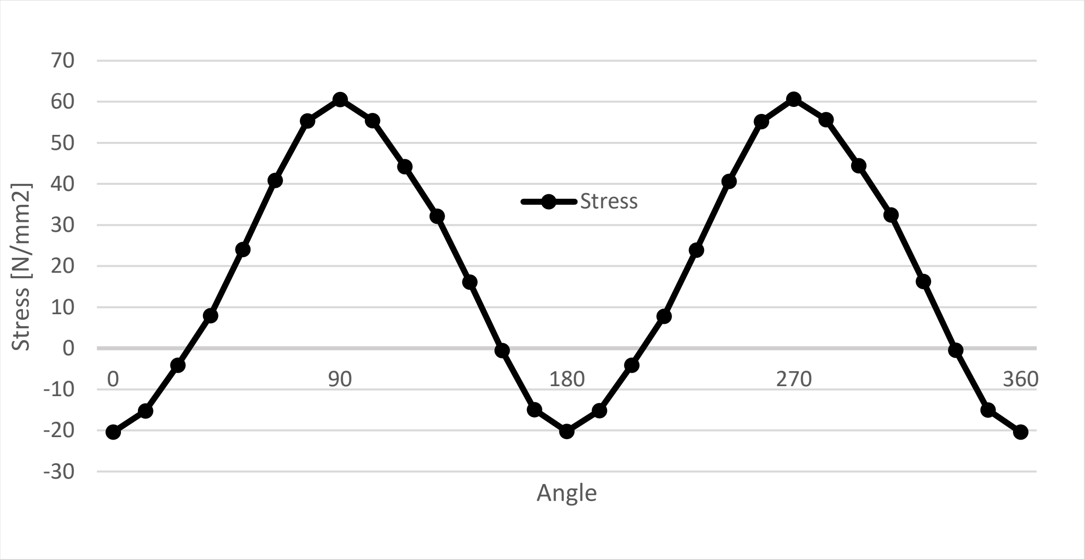

Figure 4-2: Circumferential stress around the void

In addition, the result of the von Mises stress distribution of the same problem is shown in figure 4-3. Again, the extreme stress values appear around the void. The maximum and minimum stress values are 60,3 N/mm^2 and 1,6 N/mm^2, respectively. In the regions close to the void, a local pattern of the stress field can be recognized where there are significant increases and decreases of the stress values. This is highlighted by the dark blue, green, yellow and red colours in the figure. In the regions further away from the void the stress values reach a relative constant value, which is equivalent to the nominal stress. This is easily identifiable by the light blue colour in the figure. There is a definite sign of the nominal stress. There is slight fluctuation around the stress value of 20 N/mm^2, that leads to a similar stress concentration factor as above.

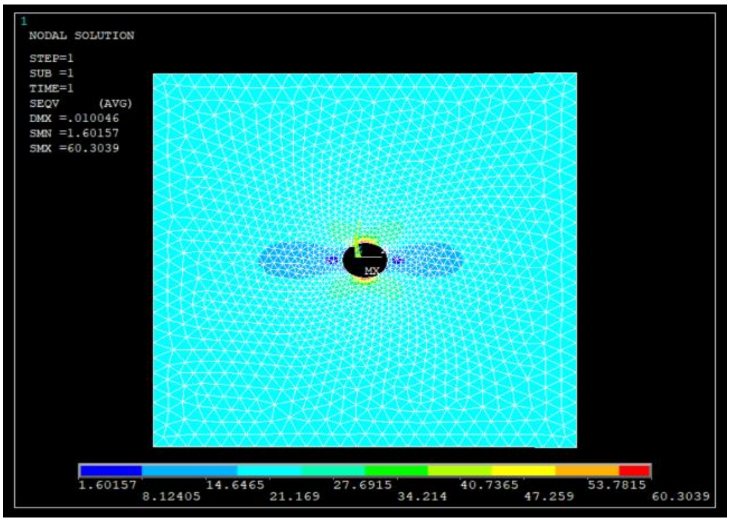

Figure 4-3: Triangular smartsize mesh of 2D plane with 5mm void (von Mises)

The simulation is now repeated with refined mesh and the maximum stress is noted. The diagram below (fig. 4-4) demonstrates maximum stress depending on the element number. Both the maximum circumferential and von Mises stress show small rises for the first instances of refinement. Thereafter, the maximum stress is converging towards a constant value.

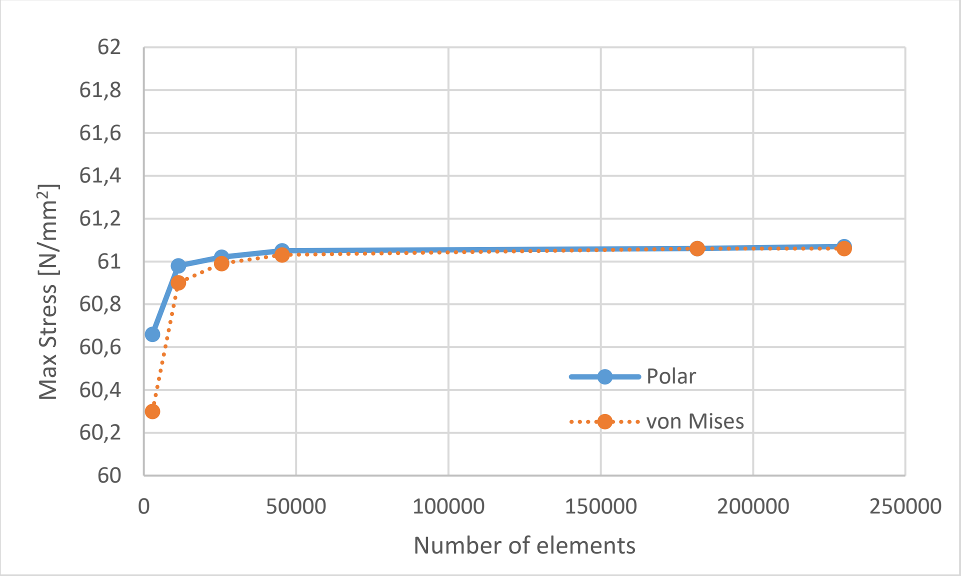

Figure 4-4: Convergence diagram of the maximum shear stress and von Mises stress

Another way of looking at the problem, is by plotting the vector field of the stress as illustrated in figure 4-5. At each node there is a vector represented by arrows, whose magnitude is determined by the length and colour of the arrows. It is important to highlight that the arrows exist in both directions due to the tensile loading of the structure. The number of arrows is increasing, the closer the distance is towards the void. The direction of the vectors is initially vertical in X-direction at the edges, but when nearing the void the vectors deflected around it. Exactly at the void large vector sizes can be seen, which implies large stresses. Blue coloured arrows can also be seen around the void, where the arrows point towards each other, which is a hint of compressive stress.

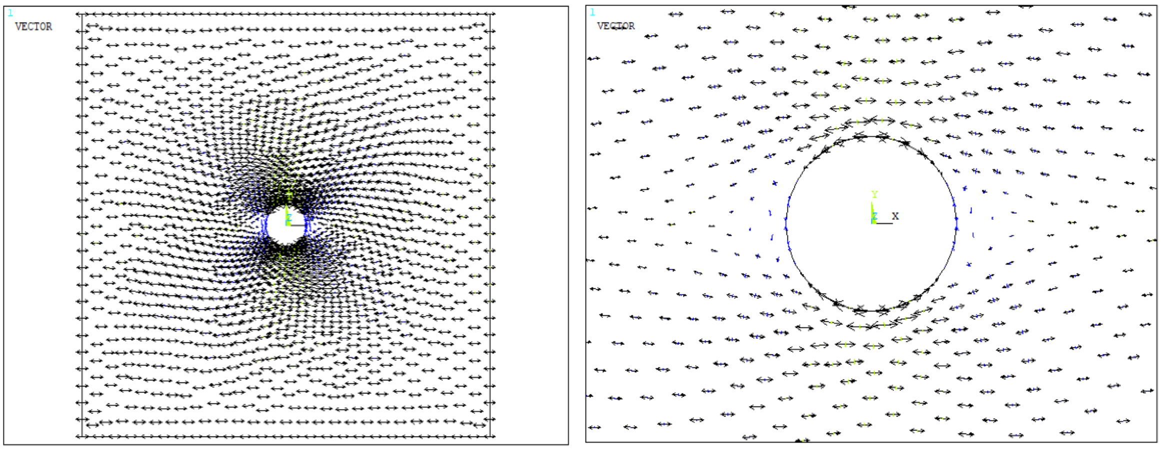

Figure 4-5: Vector plot of 2D plane with 5mm void. a) Complete structure b) zoom of void

The course of the circumferential stress around the void (fig. 4-2) matches very well with analytical solution from chapter 2.5 (fig. 2-9). Only the values differ slightly, such as the stress concentration factor of 3,03 being marginally greater than the analytical stress concentration factor. This has likely been caused by the fact, that the plane is not infinite. Although uniform stress unfolds, the finite edges still have a minimal influence on the void.

Plotting the stress in polar coordinates is very reasonable for the stresses around the void. However, for the rest of the plane structure it is rather unfitting, since its very coordinate dependent. Especially far away from the void, it is questionable to determine if uniform stress occurs from the circumferential stress plot (fig. 4-1). On the contrary, the von Mises stress plot (fig. 4-3) clearly shows stress uniformity, but the compressive stress (negative stress) around the void is not depicted due to the formula for the von Mises stress. Nevertheless, the maximum stress in polar coordinates and the von Mises maximum stress around the void possess very similar values. This can also be seen in the convergence diagram, where for large element numbers both stress values become identical. The vector plot (fig. 4-5) compares well to the force lines (fig 2-7) from chapter 2.5. At 90° and 270° degrees around void the vectors are concentrated, while at 0° and 180° there is a compressive stress.

4.2 2D - Mapped meshing

Another way of solving the 2D problem is by using mapped mesh. However, the geometry needs to be setup in such a way where mapped meshing is possible. Figure 4-6 show the 2-D plane with mapped mesh, with the circumferential stress distribution in angular polar direction. A characteristic of the mapped mesh is that the elements are symmetrically located in straight lines from the edges towards the void. The elements get smaller along the lines towards the void. The maximum stress in this case of a 5mm void reaches a value of 56,26 N/mm^2 or a stress concentration factor of 2,81. Again, it will be assumed that calculating the stress concentration factor is possible,

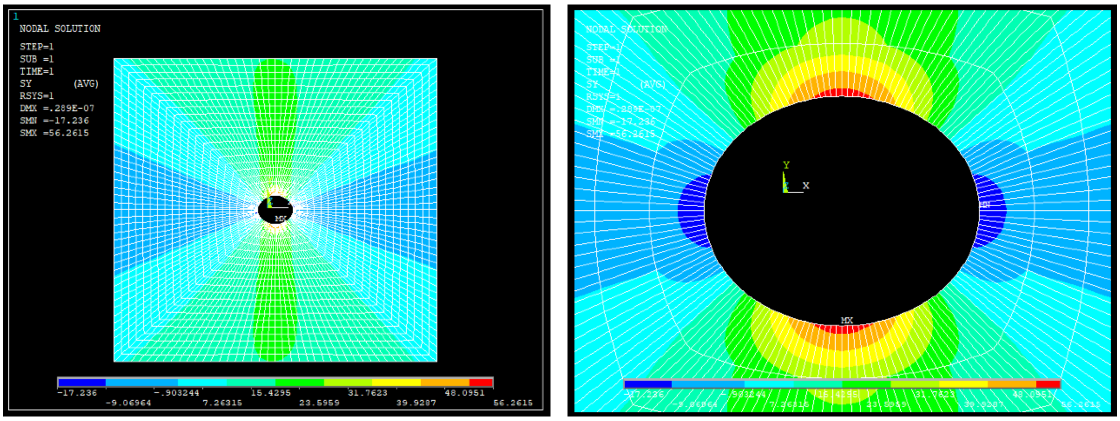

Figure 4-6: Rectangular mapped mesh of 2D plane with 5mm void. a) complete structure b) zoom of void

The following diagram illustrates the maximum stress depending on the number of elements (fig. 4-7). Starting from a total of 800 element, the mesh will be refined multiple times and the maximum stress will be evaluated. By increasing the number of elements initially, the maximum stress or the stress concentration factor increases as well. When refining the mesh further, the line graph clearly nears a constant value. This is also known as convergent behaviour. A maximum stress value of 60,94 N/mm^2 is reached at a total element number of 320000. The equivalent stress concentration factor amounts to 3,05.

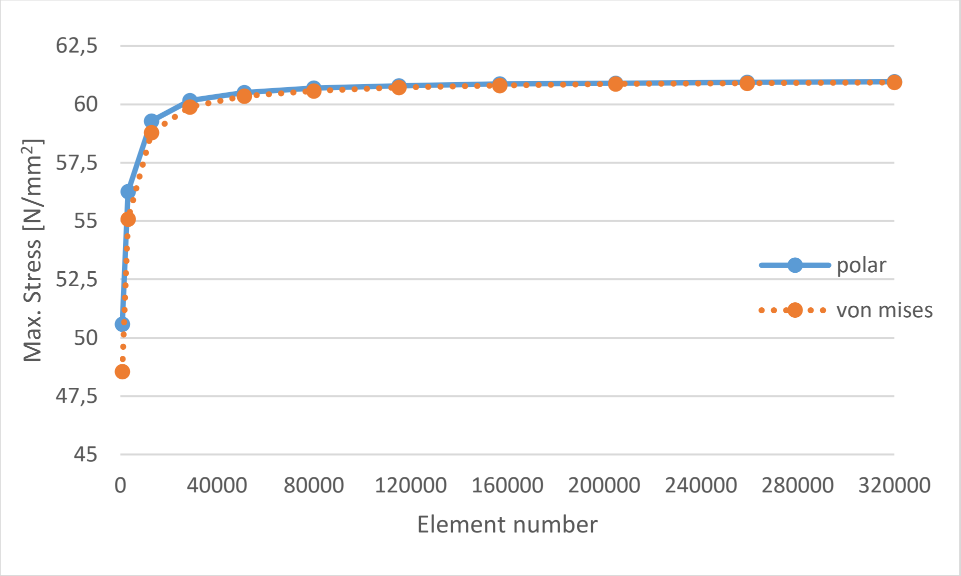

Figure 4-7: Convergence diagram of maximum shear stress and von Mises stress (mapped mesh)

A deeper look into the elements around the void shows, that they are rather long in radial direction. This characteristic remains, even when the mesh is refined. Since the stress gradients around the void are extreme, it is not ideal that a single element covers multiple stress levels. As can be seen in the diagram (fig. 4-7) the maximum circumferential stress and the von Mises stress values become more identical with increasing elements used in the simulation. Without refinements, the maximum stress value differs greatly from the convergence value.

As a result, the mapped mesh will no longer be considered for further simulations, because the smartsize mesh is not only easier to use, but also provides better results optically and practically with and without refinement for this specific problem.

4.3 2D - Variable void size

In this section the void size will differ, but the plane size of 100mm x 100mm will remain the same. For large void sizes, the nominal stress is either very difficult to determine or it does not exist. Hence, the stress concentration factor is omitted. Thus, the respective maximum stress will be measured of all simulations. Starting from a radius of 1mm, the void size will then be simulated at 5mm, 10mm and further in 5mm steps until 40mm. Figure 4-8 shows the stress fields for the circumferential stress (left side) and the von Mises stress (right side) for the sizes 1mm (upper figures), 10mm (middle figures) and 25mm (lower figures). The displayed colours are relative to their own stress scale bar and should not be compared between the figures.

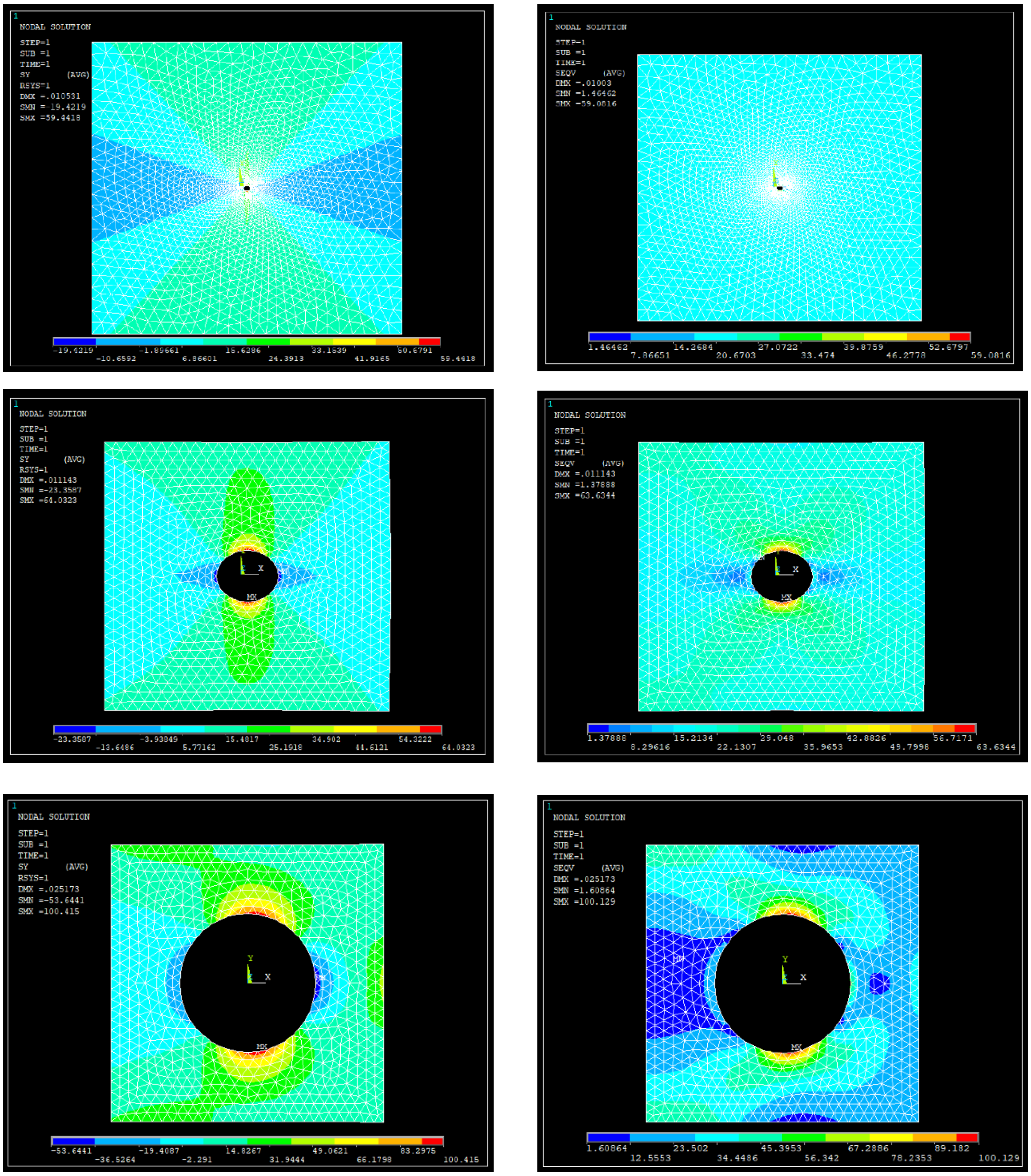

Figure 4-8: Simulation of different void sies. a) circumferential stress 1mm void b) v. Mises stress 1mm c) circumferential stress 10mm void d) v. Mises stress 10 mm void e) circumferential stress 25mm void f) v. Mises stress 25mm void

A uniform stress unfolds at small void sizes at a distance away from the void, especially in the case of the 1mm void. While the plot of the von Mises stress indicates complete uniformity of the distributed stress at a small distance away from the void, the plot of the circumferential stress shows a different kind of uniformity, due to the coordinate system. At 0° degree the angular coordinate is perpendicular to the tensile loading direction, whereas at 90° degrees the directions are aligned and therefore gives a better representation. This is highlighted by the light-green zones, where the stress reaches a constant value of 20 N/mm^2, in fact the value of the nominal stress. This is still the case in the example of the 10mm void, where the uniform stress is just about reached in both cases. The so-called local zone around the void is almost reaching the edges of the plane. Increasing void size also extinguishes the uniformity at a constant plane size as shown in the two latter figures where the 25mm void are displayed.

Large void sizes present a greater influence on the entire plane. Hence, the stress concentration factor cannot be determined theoretically. Instead, the maximum stress is plotted over the diameter / edge length ratio (fig. 4-9).

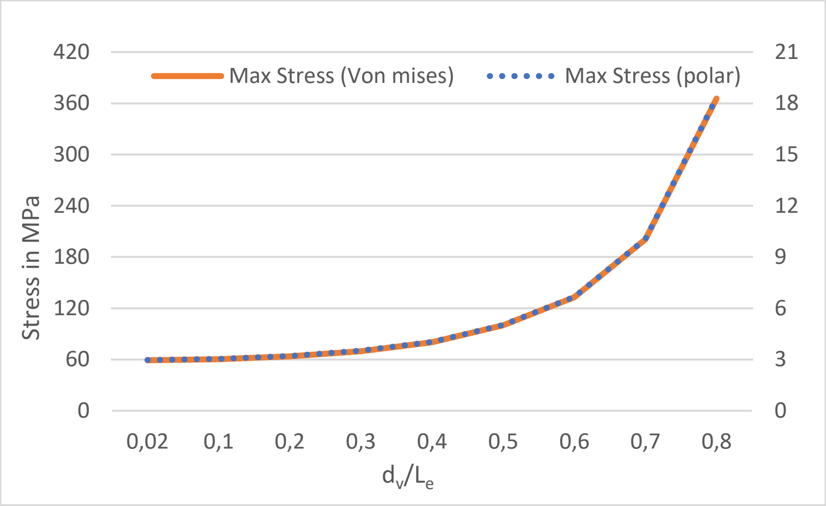

Figure 4-9: Maximum stress of the different void sizes

It can be noticed that the maximum stress remains constant at 60 N/mm^2 initially, when a stress of 20 N/mm^2 is applied, which results in a stress concentration factor of 3. At a void radius of 10mm or a diameter /edge length ratio of 0,2 the maximum stress starts to increase. In the figure 4-8d the local zone created by the void almost exceeds the edges of the plane. Further increase of the void radius leads to exponential growth of the maximum stress. The locations of the maximum stress remain around the void at 90° and 270°, initially. For great void, these locations drift towards the load side, as seen in figure 4-8e and 4-8f. The values of the maximum crcumferential stress in polar coordinate and the maximum von Mises stress are almost identical throughout the entire diagram.

The areal porosity for different void sizes has been calculated with the help of formula (2) and is presented in table 2 along with stress concentration factors of the simulation (fig. 4-9) and analytical solution (fig. 2-9). Furthermore, the error between the values has also been calculated.

Table 3: Stress concentration factor of a 2D plane with variable circular void

Radius a [mm]	Diameter / edge length ratio d_v/L_e	Porosity Φ_{Ar} [%]	Stress concentration factor (Simulation, v. Mises stress)	Stress concentration factor (Literature)	Error percentage [%]
1	0,02	0,03	2,95	3	1,67
5	0,1	0,79	3,02	3,03	0,33
10	0,2	3,14	3,18	3,14	1,27
15	0,3	7,07	3,49	3,35	4,18
20	0,4	12,57	4	3,69	8,4
25	0,5	19,63	5,01	4,25	17,88
30	0,6	28,27	6,65	5,16	28,88
35	0,7	38,48	10,04	6,76	48,5
40	0,8	50,27	18,28	10,04	82,07

The results of the variable void size can be explained with the help of the force lines principle. As the voids get bigger, the deflections increase as well which results in more force lines passing around the void. While the plane size remains the same, the edges restrain the force lines from deflecting. The deflected lines become denser in addition, which ultimately leads to a higher stress. The reason of the similarity between the maximum stress in polar coordinates and the von Mises stress is that around the void the radial stress is zero. Therefore, the circumferential stress in angular polar direction is the only term in the von Mises formula.

The values for the stress concentration factors from the simulation and analytical solution are very similar, initially. The error in percentage is very low for small diameter / edge length ratios until 0,2. From a ratio of 0,2 until 0,4 the stress concentration values begin to deviate as evident in the error percentage. Above the ratio of 0,4 the true stress concentration factor can not be calculated, neither in the simulation nor the analytical solution. The values have been calculated regardless for the sake of completeness since the maximum stress in the simulation is known and the formula from the analytical solution. However, these values should not be considered and are therefore marked red in table.

4.4 2D – Void position

The position of the void inside the plane is of major importance. In this section, the position will be varied in fixed directions and the stresses will be evaluated. Again, a single circular void with a radius of 5mm will be placed centrally in a 100mm x 100mm plane initially before the location of the void will change in the directions of the edges until the edge of each side reached. The center of the plane is also the origin with the eccentricity *e* being zero. The distance at the beginning is 45mm from all four edges. The directions are highlighted in red arrows in figure 4-10, where the right side is the loading side. To achieve a dimensionless quantity, the eccentricity *e* will be divided by half of the edge length L_e. In contrast to the previous simulation about the variable void size, the stress will stabilize far away from the void in all cases. Due to this reason, the stress concentration factor can be measured.

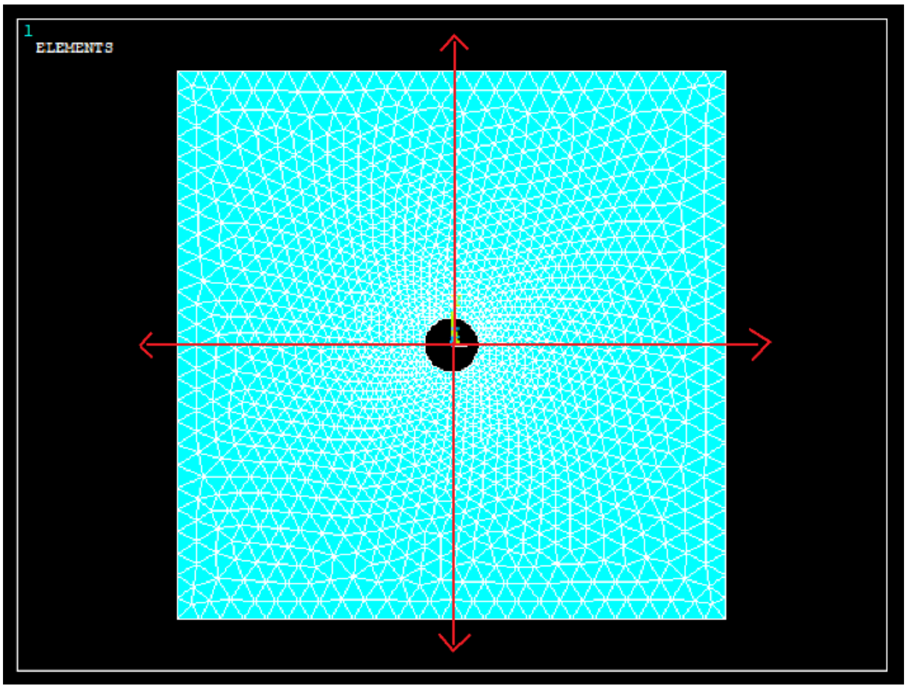

Figure 4-10: Void directions

The stresses for each step were evaluated and divided by the related nominal stress, which in all cases can be assumed 20 N/mm^2, which ultimately results in the stress concentration factor. The results are displayed in the diagram below (fig. 4-11).

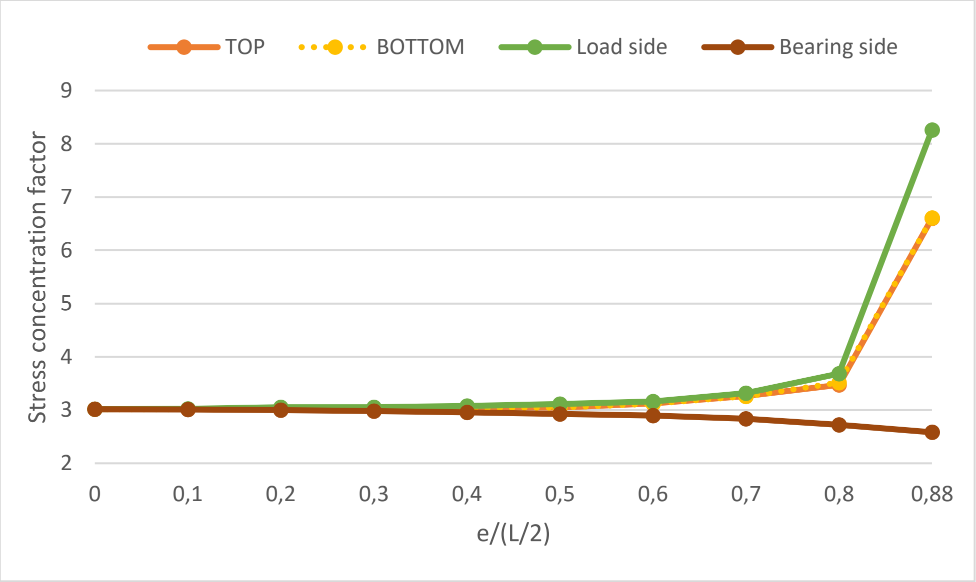

Figure 4-11: Stress concentration factor of variable void position

Until the ratio of 0,4 all simulations show a constant stress concentration factor of 3. From 0,4 to 0,8, there is a slight increase of the stress concentration factor and from 0,8 to 0,88 the stress concentration factor increases rapidly, when the void is moved towards the top, bottom and load side edge. Plotting the void near the bearing side, a slow decrease is measured from 0,4 to 0,88.

At a distance of 1mm or a ratio of 0,88 from the loading side edge, a stress concentration factor of 8,26 can be measured. The same distance away from the top and bottom edge results in a stress concentration factor of 6,6. The results throughout all distances for the top and bottom edge are almost identical. When the void is placed 1mm away from the bearing side, the stress concentration factor falls to 2,58.

Figure 4-12 displays the example of the void 1mm near the load side void. A maximum stress of 165,23 N/mm^2 can be seen from the stress scale bar. Far away from the void, the stress values fluctuate around the value 20 N/mm^2, which is the nominal stress.

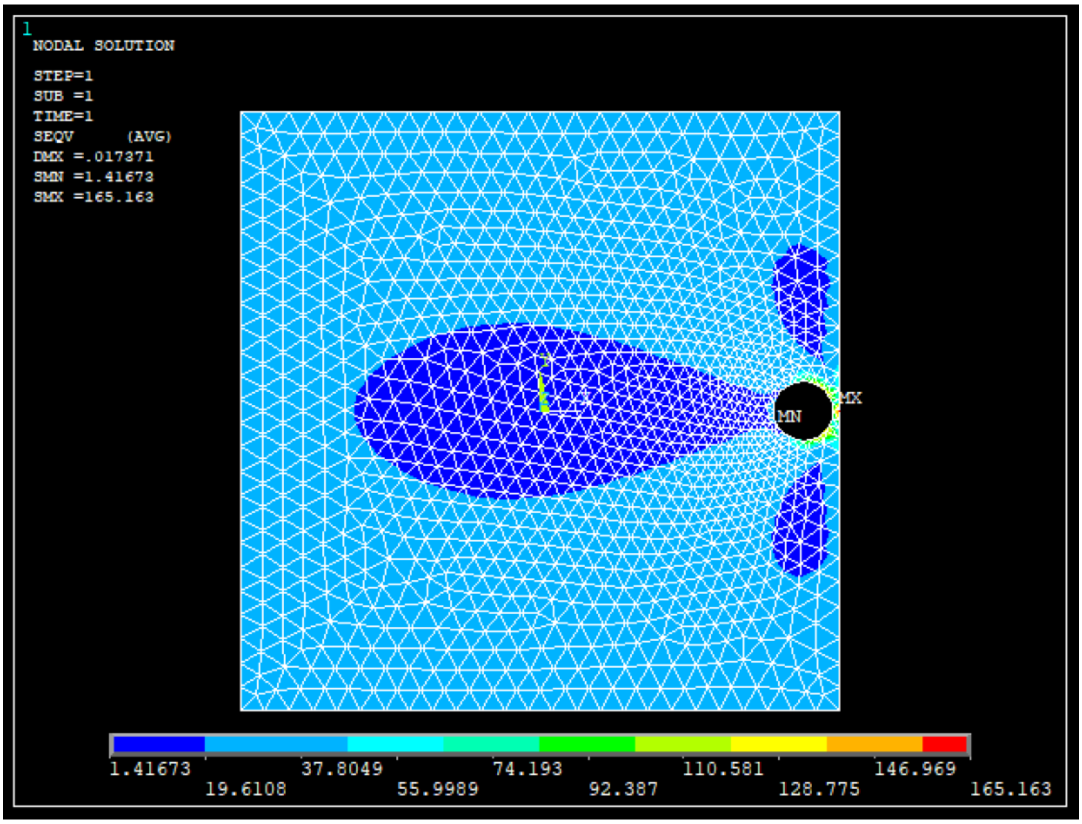

Figure 4-12: Simulation of the von Mises stress distribution of a 5mm void 1mm away from the loading side edge

The results of this chapter show that simulating with a load side and a bearing side is not exactly the same as having two load sides like the analytical solution. Void stresses are more critical towards the loading side. However, simulating with two loading sides cannot work in ANSYS. Using boundary conditions are essential for structural analysis in ANSYS. Only for voids with an eccentricity ratio above 0,4 from the origin, a noticeable difference exists. Up until that distance the differences in the values are negligibly small.

4.5 2D - Elliptical hole

The simulation is performed with an elliptical hole instead of an concentric circular one. The major and minor axis will be oriented both in tensile direction and perpendicular to the tensile direction. Different geometries of the ellipse will be applied, however, the ellipse will remain very small in comparison to the 100mm x 100mm 2D plane, to minimize the effects of finite edges. Smartsize meshing will be used for all simulations with a single elliptical hole.

The formula for the maximum stress of an elliptical hole has already been mentioned in chapter 2.6, where the maximum stress is linear proportional with the term a/b:

$$\sigma_{max,El} = \sigma * (1 + 2 * \frac{a_{El}}{b_{El}}) \qquad (11)$$

With a being the radius of the axis perpendicular to the load direction and b being the axis in line with the load direction. Figure 4-13 illustrates a plane with an elliptical hole, where the tensile load is applied in the right and left edge. In the example of a_{El} = 4mm and b_{El} = 1mm, the maximum stress value of 178,58 N/mm^2 can be taken from the figure.

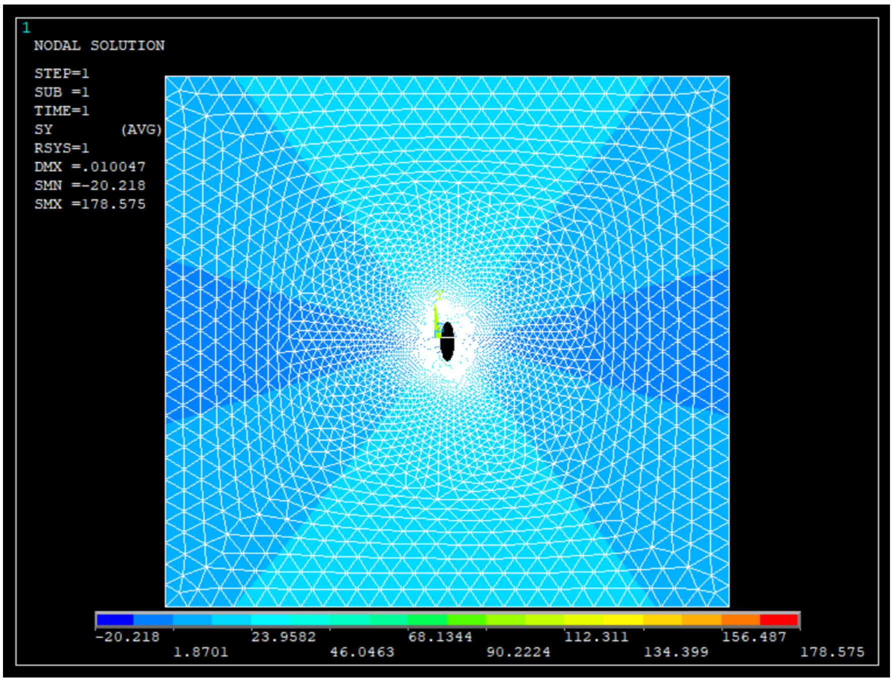

Figure 4-13: Circumferential stress distribution of 2D plane with an elliptical void

The formula as well as the maximum stresses from finite element simulations have been plotted over axes ratio a_{El}/b_{El} and are illustrated in figure 4-14. The value of the axis b_{El} remain constant at b_{El} = 1mm, while the axis a_{El} is being varied from [0.25 ; 4] in 0.25mm steps.

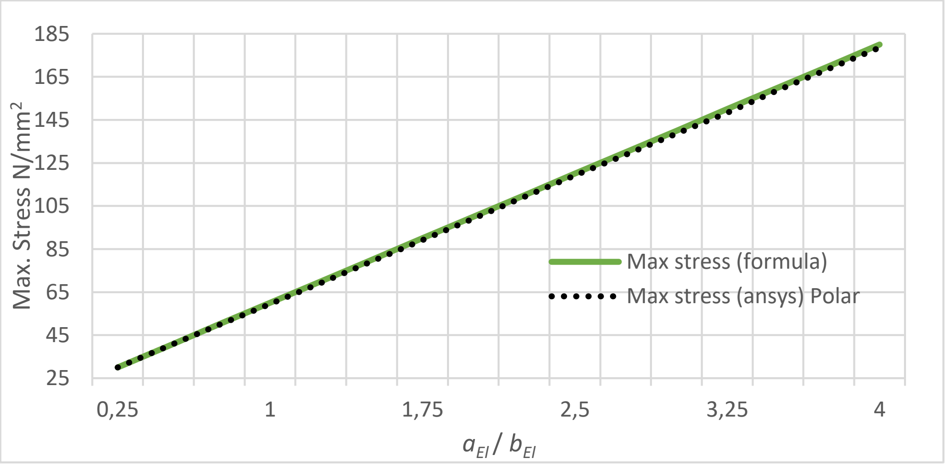

Figure 4-14: Maximum stress of an elliptical hole (diagram)

Both line graphs clearly show a monotonous linear rise and are almost identical. At the starting axes ratio of $a_{El} / b_{El} = 0.25$ the formula as well the simulations provide a maximum stress at exactly 30 N/mm^2. With increasing axes ratio, a marginal deviation can be seen between the analytical maximum stress and maximum stress from the simulation.

Elliptical holes that are fully circular help understanding the principle of the force lines further. The orientation as well as the size play a role when determining the maximum stress. If the major axis stands perpendicular to the tensile load direction, the deflection of the force lines is greater. At the same time the range or width of the deflection remains small compared to a circle. Furthermore, the tip radius of the ellipse, where the deflected force lines pass through is small. This leads to very dense force lines and a greater maximum stress because it is more of an abrupt change. On the contrary, when the minor axis is located perpendicular to the load direction, the deflection is smaller, it takes place over a greater range and the radius. The force lines experience a smoother path which results in lower stresses.

4.6 2D – Multiple voids

To determine the influence of a second void, the first void remains centrally placed in the middle of the 100mm x 100mm plane, while the second void will be rotated around the first void from 0° degrees to 360° degrees in fixed distances.

In the figure 4-15, an example is shown of the second void, that is located at a distance of 10mm and at an angle of 0° from the first void. The rotation of the angle works in counterclockwise direction. The tensile load will remain with a value 20 N/mm^2.

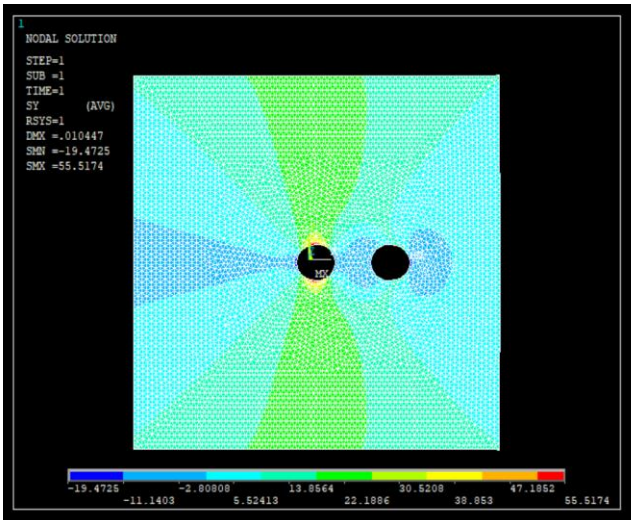

Figure 4-15: 2D plane of a second rotating void (10mm distance and 0° degrees)

The maximum circumferential stress of the first void is evaluated. At a distance of 5mm and 10mm between the voids, the second void was rotated. The results are shown in figure 4-16:

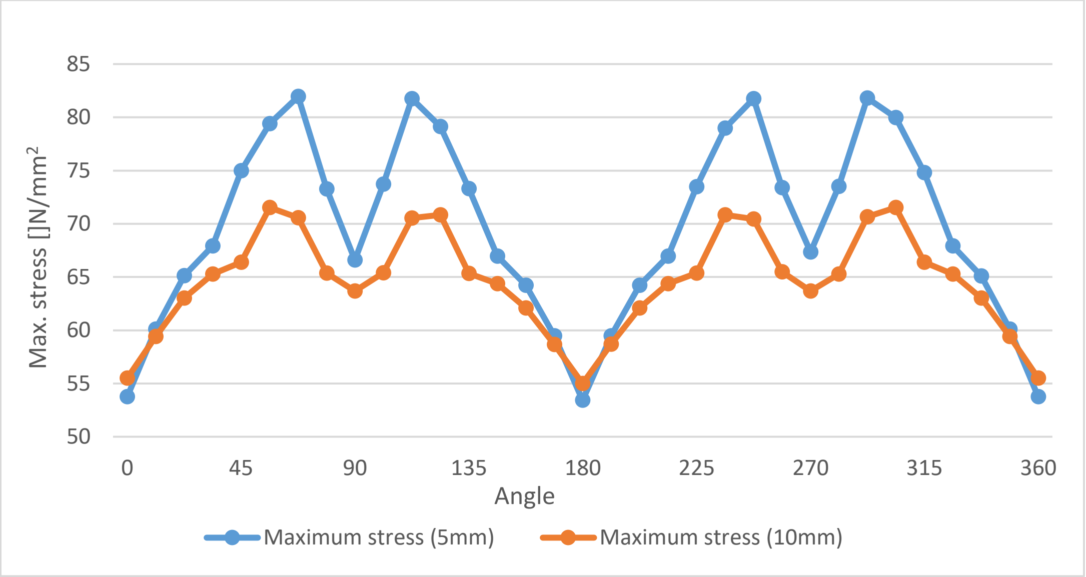

Figure 4-16: Maximum circumferential stress of central void with rotating second void (diagram) in fixed distances: 5mm (blue curve), 10 mm (orange curve)

Both graphs show not only a symmetric but more or less a periodic behavior, with 180° or π being one period. At a distance of 5mm to the second void (blue curve), the global maximum stress of 81,95 N/mm^2 can be detected at an angle of 67,5° degrees. Other peak maxima points can be seen at 112,5° degrees, 247,5° degrees and 292,5° degrees, respectively. Their values are just slightly below the value of the 81,95 N/mm^2. At 0°/360° and 180° the global minima are portrayed with the lowest maximum stress value of 53,42 N/mm^2 situated at 180°. From 0° degrees onwards there is a monotone increase of the maximum stress until 67,5° degrees, which is the first peak. Thereafter, the maximum stress decreases until the two voids are in a angle of 90° degrees to each other, where a local minimum with a stress value of 66,61 N/mm^2 can be noticed. Exceeding 90° degrees, the stress grows until the second peak maximum point at 112,5 degrees. Beyond the second maximum peak, the maximums stress drops to the minimum at 180° degrees. The course of the curve from 180° degrees to 360° is almost identical to the course from 0° degrees to 180° degrees. The figure 4-17 below shows the void constellation leading to the highest maximum stress in the diagram, which occurs when the second void is located at a angle of 67,5° degrees to the central void.

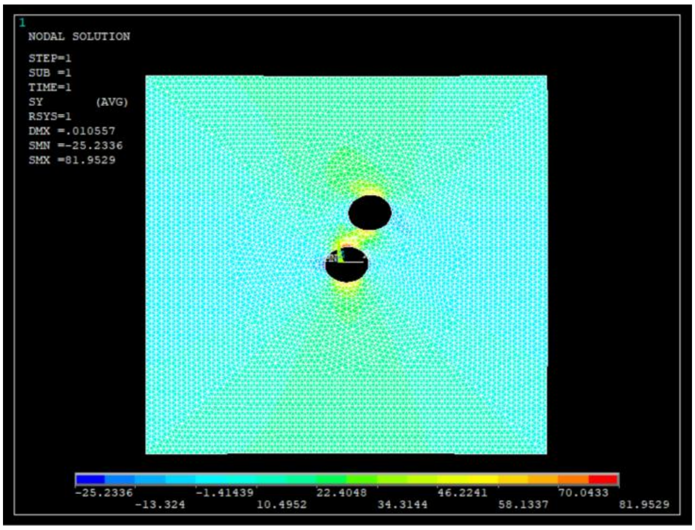

Figure 4-17: 2D plane of a second rotating void (5mm distance and 67,5° degrees)

Another way to look at this exact situation, is by plotting the vector plot around the two voids as in figure 4-18. The direction of the vectors is initially uniform, before nearing the two voids, where the deflection begins. Especially the area between the two voids is critical. The length of the vectors is greater, which indicates that the stresses are higher. In addition, a large amount of the vectors is deflected greatly, while the second void still being near the maximum stress location of the first void.

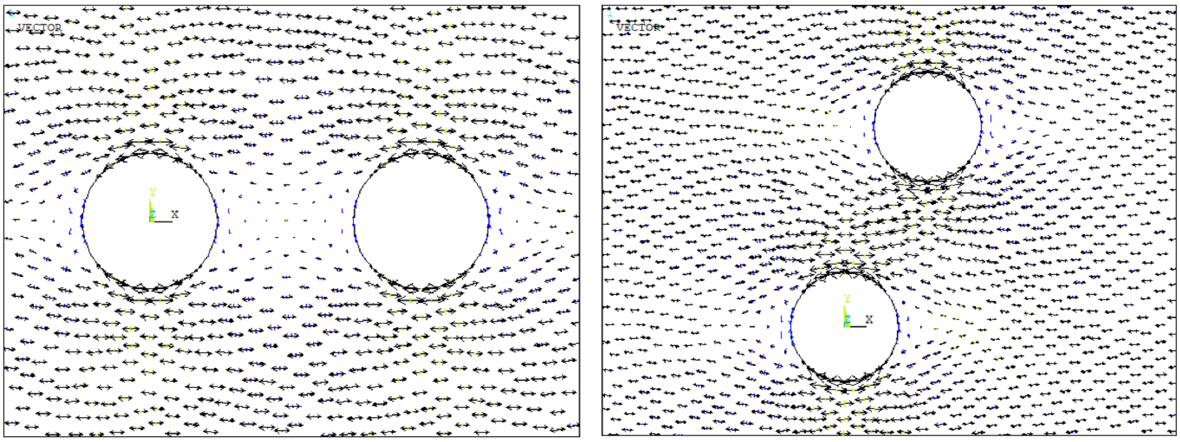

Figure 4-18: Vector plots of 2D plane with second rotating void. a) 10mm distance and 0° degrees. b) 5mm distance 67,5° degree

The same procedure has been done for a void distance of 10mm and evaluated in figure 4-16 as well (orange curve). Again, the graph is symmetric and has a similar course as the previous graph. However, the maximum peak stresses are significantly lower, with the highest maximum stress value being 71,53 N/mm^2. In fact, all values are lower regarding the angle position, with the exception of the lowest maximum stresses of 55,52 N/mm^2 and 54,99 at 0°/360° and 180°.

These stresses are higher than the lowest maximum stresses of the simulation, where the second void is closer to the first (blue curve). The angles, in which these maximum peak stresses occur are at 56,25° degrees, 123,75° degrees, 236,25° degrees and 303,75° degrees. These angles are different to the ones from the previous simulation, where the void distance is 5mm.

It was anticipated that a second void closer to the first void would generate higher maximum stress. This is also the case for all angles except for at 0° degrees and 180° degrees, where the second void, which is further away causes a greater maximum stress. At these angles, the voids are placed in line with tension load direction and the maximum stress are less than 54 N/mm^2 in both cases. This is in fact lower than the maximum stress of a single void. In a plane with a single void, force lines that are deflected are immediately deflected back once the void has been passed. The presence of a second void in tensile direction makes the force lines pass through second void also, before being deflected back in order to achieve uniformity. Depending on the distance between the voids more or less force lines are deflected back immediately after the first void. In case both voids are very close to each other, barely any force can pass through in between the voids. This is a more smooth transition in comparison to a single void, which reduces stress as evident in the results. For these angles, the maximum stress is lower the closer voids are.

The four global maximum stress points occur at angles that are symmetric to each other in regards to the X-axis and Y-axis. Therefore, similar values are obtained. From 0° degrees to 90° more and more force lines are passing through the gap between the voids. At these specific angles the force lines that pass through in between the voids become critical. In the example of the second void being located at 67,5° degrees and 5mm from the first void (fig. 4-18), the force lines that are deflected upwards due to first void are experiencing a second immediate deflection because the second void. For angles between 67,5° degrees and 90°, the deflection of the force lines decreases which reduces the maximum stress. At exactly 90° degrees the deflection is minimal, which explains the local minimum. From 90° to 180° degrees the procedure is reversed.

4.7 3D - Single void

At first, the size of the single spherical void is being varied inside the cylinder. It is to be noted that for a small void size a uniform will result in far distances away from the void. However, for a large void radius the simulation will not result in uniform stress distribution. Therefore, the maximum stress will be calculated and not the stress concentration factor. In the figure 4-19, a diagram displaying the change in maximum stress (blue curve) by using different void sizes can be seen. In addition, the number of elements used in the associated simulation (orange curve) is also depicted. These parameters are plotted over the relation of the void radius a_{sph} divided by the constant cylinder radius R_{cyl}.

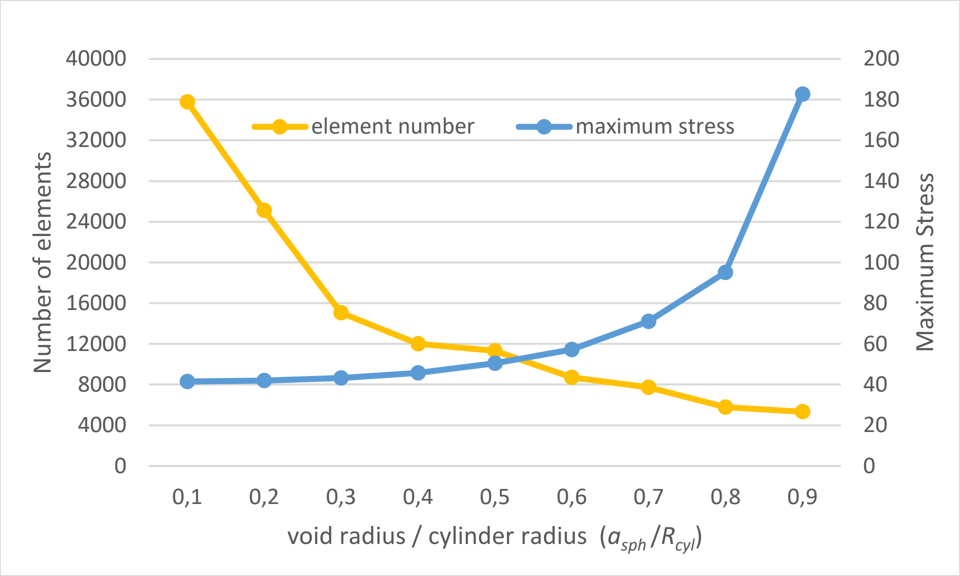

Figure 4-19: 3D cylinder with single spherical void. Void size and element number (diagram)

At the lowest radius ratio of 0,1 the maximum stress has the value 41,5 N/mm^2. There is a very slow rise in the maximum stress until a radius ratio of 0,4. Afterwards the slope keeps increasing after each step. At a radius ratio of 0,9 the maximum stress has reached a value of 182,76 N/mm^2. Table 3 shows the porosity percentage and the stress concentration factors of the simulation and with increasing void radius:

Table 4: Stress concentration factor of 3D cylinder with variable spherical void

Radius r [mm]	**Void radius / cylinder radius ratio a_{sph} / R_{cyl}**	**Porosity Φ_{Vol} [%]**	**Stress concentration factor (Simulation)**	**Stress concentration factor (analytical)**	**Error percentage [%]**
5	0,1	0,07	2,075	2,05	1,21
10	0,2	0,53	2,094	2,07	1,18
15	0,3	1,8	2,16	2,11	2,38

20	0,4	4,27	2,288	2,19	4,48
25	0,5	8,33	2,519	2,33	8,13
30	0,6	14,4	2,862	2,65	7,98
35	0,7	22,87	3,55	-	-
40	0,8	34,13	4,76	-	-
45	0,9	48,6	9,134	-	-

The number of elements is decreasing with increasing radius ratio. This is due to the fact, that the overall cylinder volume decreases as well. Therefore, less and less elements are being used.

The following figures 4-20 display the simulation results of a 5mm void inside the cylinder. In order to visualize the void, the cylinder has been cut in the middle perpendicular to the tensile direction and in tensile direction. This has been done in the post-processing step.

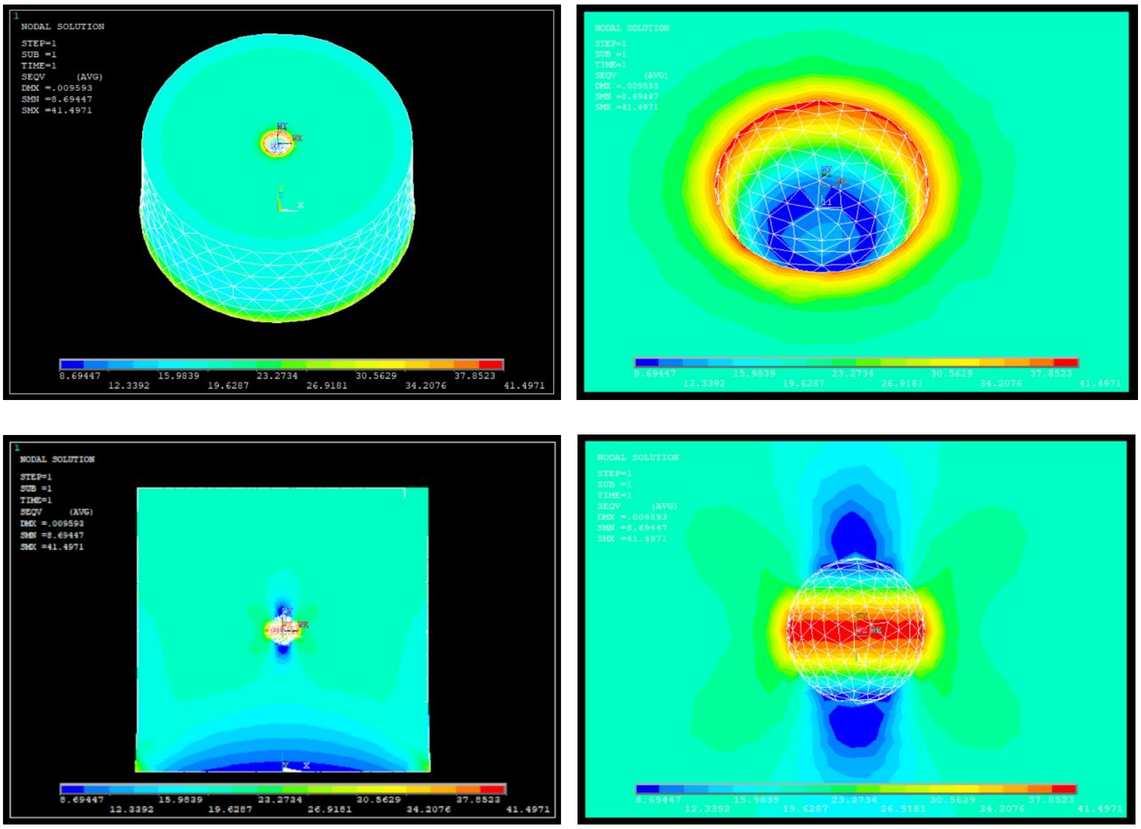

Figure 4-20: 3D cylinder with single spherical void. a) Horizontal cut; b) horizontal cut (zoom); c) vertical cut; d) vertical cut (zoom)

The use of smartsizing mesh can be identified clearly. The size of the element on the outer shell surface is rather large in contrast to the element size used for the void, which is relatively small. The maximum stress amounts to 41,5 N/mm^2 and is located at the inner surface of void. In this particular case, the stress concentration factor can be calculated, since the stress stabilizes itself further away from void. The result is:

$$K_t = \frac{\sigma_{max}}{\sigma_{nom}} = \frac{41{,}5\ N/mm^2}{20\ N/mm^2} = 2{,}08 \qquad (13)$$

A closer look inside the void reveals that a complete ring of an area displays the red colour, which is an indication of the highest stress inside the structure according to the scale for this load case. The middle axis of the ring is aligned with the tensile direction of the load. The high stress however quickly fades away when moving away from the void. The void also exhibits areas, where the stress is significantly lower than the applied stress. These areas are still visible close to the void. Altogether the areas of high and low stresses due to the void appearance emerge into a local field of its own. However, the lowest stress value is located at the bottom of the cylinder with a value of 8,7 N/mm^2.

It was anticipated that the maximum stress would be distributed at the equator of the void, since the 3D problem is just a rotation of the 2D problem. However, the stress concentration factor for a cylinder with a single fully spherical void is significantly lower compared to 2D plane with circular void. A drop of over 30% can be calculated. The force lines in the 2D plane could only be deflected in one direction and had to stay in the plane. In the case of the 3D cylinder the force lines can be deflected in any direction. Furthermore, the maximum stress in 3D is distributed in ring shape around the void instead of two very small regions in the 2D plane. These factors are likely to be the reason for the reduction of the stress concentration factor.

It is no surprise that the maximum increases rapidly when the void size is raised as well. The greater the void, the more force lines are deflected while the outer geometry dimensions remain the same. Like the 2D-problem, the finite edges are responsible for rapidly increasing the stress when the void radius increases.

The stress concentration factors between the simulation (fig. 4-19) and analytical solution (fig. 2-12) for a 3D cylinder with a spherical void differ very little with increasing void size. This is also supported by the error percentage, that remains low throughout the different void sizes. Above a void radius / cylinder radius ratio of 0,6, there is no data for the analytical solution and above a ratio of 0,5 the curve is dotted (fig. 2-12). Therefore, the values are marked red.

4.8 3D – Multiple voids - Rotation

Next to the centrally placed void, a second void will be added and rotated around the first void. In the figure 4-21, two coordinate system can be noticed. The global coordinate system with the axes X, Y and Z is located at the bottom of the cylinder. Because of ANSYS APDL modelling reasons, a second work plane with the axes WX, WY and WZ is introduced in order to create the void. The work plane is translated by 50 mm from the global coordinate system along Z-axis. The center point of the second void is placed 15mm in WX-direction with a minimum distance of 5mm to the first void, which marks the starting point of zero degrees. The second void is then rotated entirely around the WZ-axis and then around the WY-axis and the results are obtained. The maximum stresses over 360° degrees are displayed in the diagram in figure 4-22 for each rotation. The cylinder has been cut through the WX-WY-plane to visualize the rotation around the WZ-axis, and a cut through the WZ-WX-axis has been made to illustrate the rotation around WY-axis.

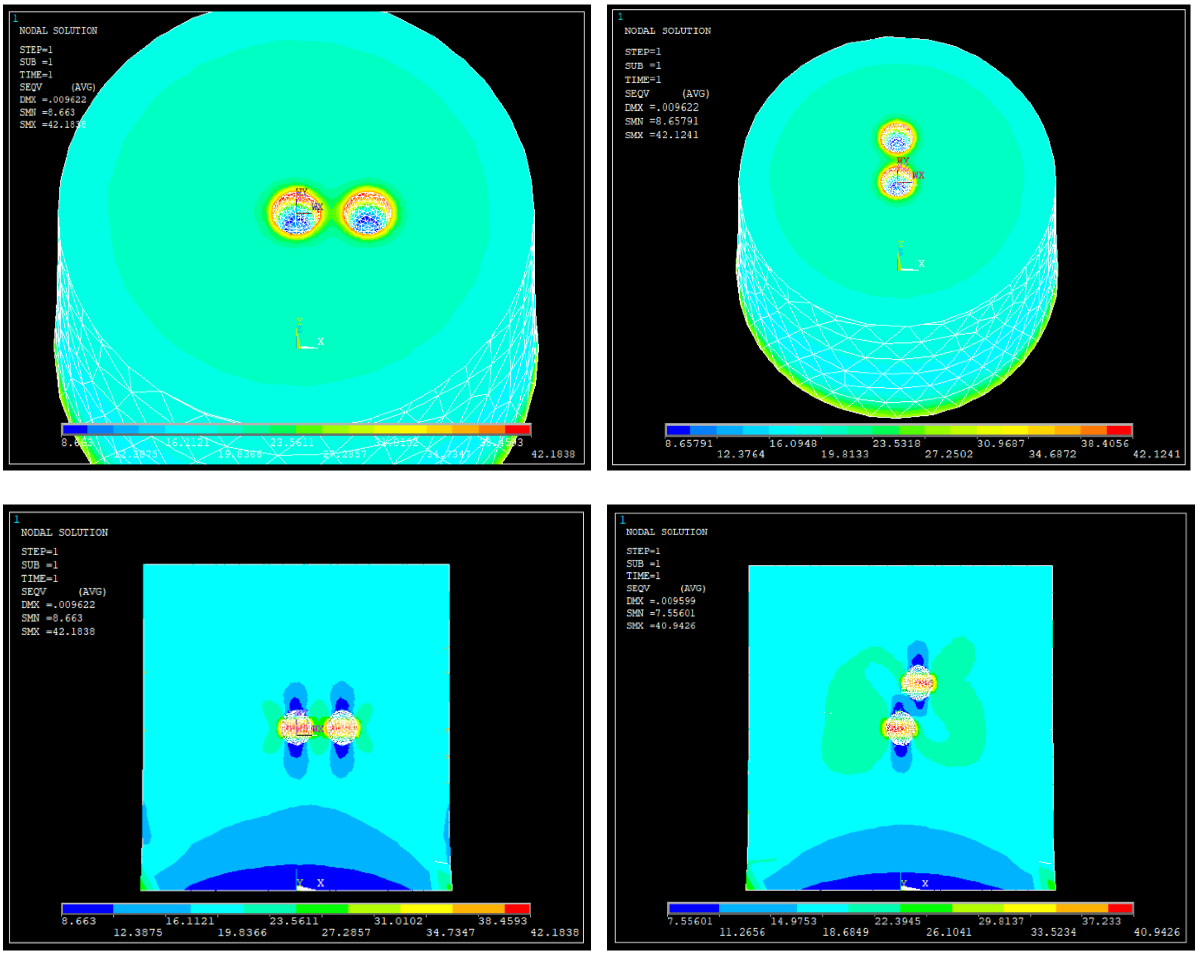

Figure 4-21: 3D cylinder with second rotating spherical void. a) Vertical cut 0° degrees Z-rotation; b) vertical cut 90° degrees WZ-rotation; c) horizontal cut 0° degrees WY-rotation d) horizontal cut 67° degrees WY-rotation

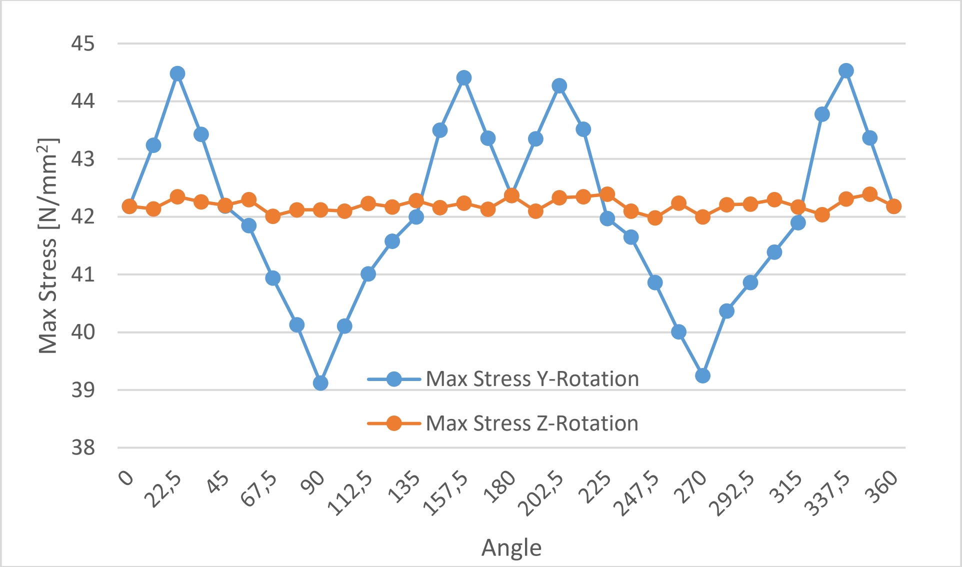

Figure 4-22: Maximum stress values over a full rotation with second void (diagram)

By rotating the second void around the WZ-axis (orange curve), the maximum stress value shows marginal fluctuations around a relative constant value slightly above 42 N/mm^2 throughout the 360° degrees. This behaviour can also be seen in the figures 4-21a and 4-21b, where the stress field remain unchanged. On the contrary, the rotation around the WY-axis (blue curve) shows both greatly increased and decreased maximum stress depending on the angle. The figures 4-21c and 4-21d are also showing this characteristic visually, as the stress field changes significantly with each simulation. The peak maximum stresses occur at 22,5° degrees, 157,5° degrees, 202,5° and 337,5° degrees with the latter being the global maximum with a stress value of 44,53 N/mm^2. The lowest maximum stress value takes place when the two voids are aligned with tensile direction at 90° degrees and 270° degrees, respectively. At 0°/360° and at 180° the simulations coincide and therefore exhibit the exact same maximum stress value.

When rotating the second void around the WZ-axis, the stress results were relatively constant throughout a full rotation, because the cylinder is axisymmetric around the WZ-axis. The first voids maximum stress is distributed at the equator around the WZ-axis. Therefore, a second void will have a similar impact on the first void throughout the entire rotation. Hence, the maximum stress does not differ that much. The fluctuation is likely to be caused using smartsize mesh. Also, the maximum stress around the equator is not constant and probably has different values, which could have been a factor for the fluctuation.

The course of the rotation of the second around the WY-axis in the cylinder is very similar to the course of the second void in the 2D-plane. In fact, there is phase-delay of 90°degrees since the starting point are not the same. In the 2D case, the second void started from when the two voids were placed along the tensile direction, which is the 0° degree point in the diagram (fig.

4-16) and a global minimum. In the 3D case, the beginning point of evaluation is, when the two voids are aligned in a line that is perpendicular to the tensile direction. The voids are not aligned along the tensile direction until 90° degrees, which is a global minimum in the diagram (fig. 4-22). The main reasons for this specific course in the 3D cylinder are identical with the reasons in the 2D-plane. At specific angles, the passage of the force lines around the voids or through the gaps between the void are more critical than others. The lowest maximum stresses occurred when the voids were aligned in tensile direction. The highest maximum stress occurred at ±67,5° degrees from where the voids were aligned in a line to the tensile load direction.

4.9 3D – Multiple voids – Translation

Voids in tensile direction along the Z-axis show reduced maximum stress. The following simulation (fig. 4-23) demonstrates the behaviour of two spherical voids inside the cylinder with increasing void distance s_V. To obtain a dimensionless quantity, the void distance s_V is divided by the cylinder length H_{cyl}. Starting at a distance of 1mm between the voids, both voids will be moved away further from each other along the Z-axis. At the smallest distance of 1mm or a void distance ratio of 0,01 the lowest maximum stress occurs with a value of 38,58 N/mm^2. In the region between the voids, the lowest stress occurs according to the figure 4-23. Thereafter, when increasing the distance until a ratio of 0,15 a slow rise of the maximum stress can be detected (fig. 4-24). From 0,15 to 0,5 void distance ratio, the maximum stress remains relative at a constant value slightly above 40 N/mm^2. Above ratio of 0,50 the maximum stress increases rapidly, with the maximum stress reaching 46 N/mm^2 at a distance of 75mm between the voids or at a ratio of 0,75.

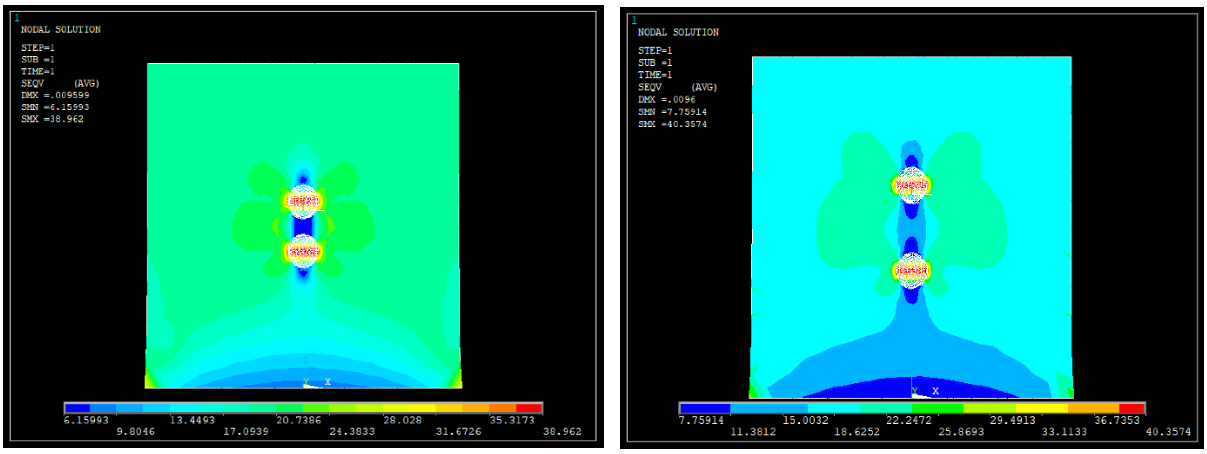

Figure 4-23: 3D cylinder with two voids translating in tensile direction

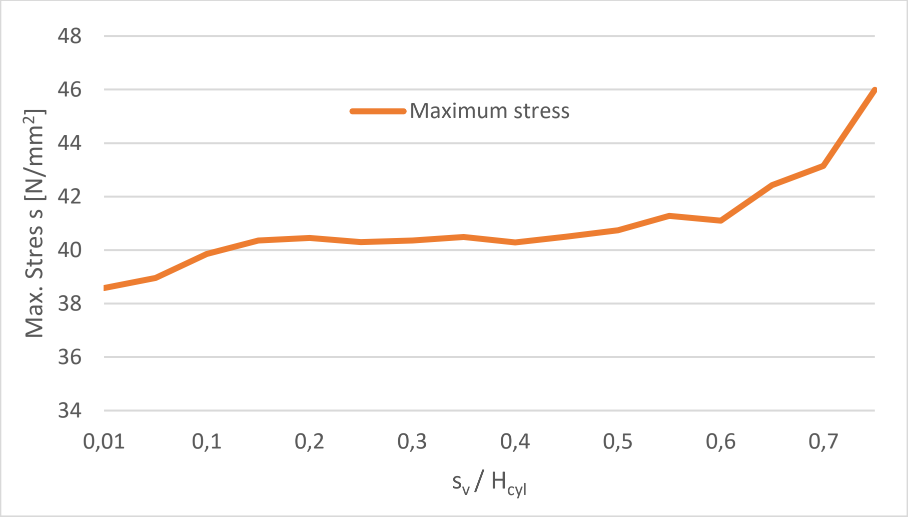

Figure 4-24: Maximum stress of two voids translating in tensile direction (diagram)

When moving the two voids in tensile load direction, the results are not surprising. The lowest maximum stress occurs when the voids distance is the shortest. The reason is similar to the 2D problem with voids. After the force lines are deflected around the first void, they are passing the second void as well, before being deflected back when the voids are too close. This relieves stress in the critical equator regions of both voids. Increasing the gap between the voids leads to a rise in the maximum stress value, because more force lines pass through the gap and burden the equator region. Exceeding the void distance ratio of 0,15 between the voids, enough force lines are deflected back immediately after passing the first void, causing no further stress addition to the equator regions. Hence, the maximum stress remains relatively constant until a void distance ratio of 0,45 as can be noted in the diagram. The exact maximum stress value bears a resemblance with the maximum stress value of a single void. For void distance ratios above 0,45 the maximum stress slowly increases further and above 0,6 a rapid rise can be detected. At these distances, the voids are very close the top and bottom surface of the cylinder, which ultimately cause the gain. However, only the void nearing the upper surface of the cylinder, which is the loading surface show the increase of maximum stress.

5 Summary and Conclusion

The main objective of this work is to research the influence of elliptical defects in mechanical structures under uniaxial tensile loading. Simulations of 2D planes and 3D cylinders with spherical pores were performed in ANSYS APDL. The maximum stress and the stress concentrations caused by the pores were particularly analyzed.

In the 2D case, a quadratic plane with a central circular void was examined. The maximum stress is located at the edges of the void, where the cross section is the least. Results showed a stress concentration factor of slightly above 3. Not only the stress concentration factor, but also the course of the stress around the void is very fitting with the analytical solution from Timoschenko (1970). When the mesh was refined, the solution converged, which is a good hint of a correct simulation.

A cylinder with a central spherical void is chosen for the 3D simulations. The maximum stress is distributed around the void at the equator of the void perpendicular to the tensile load direction. A value of 2,08 for the stress concentration factor is calculated, which compares well with the theoretical value of 2,045 [Timoschenko, 1970]. It has to noted that this exact simulation could not be tested on convergence, since the maximum element number was exceeded at the very first refinement level.

When a second void is rotated around a central void, it was found out that some angles were more critical than others. Two voids aligned in tensile load direction generates the least amount of maximum stress. At this specific constellation, voids closer to each other cause less maximum stress than void further away. This is the case for both the 2D and the 3D situation.

The position of the void proved to be critical, as well. Voids near the edges exhibit a much higher maximum stress values and accordingly a greater stress concentration factor. This confirmed the suggestion made by Yadollahi and Shamsaei (2017), that pores near the surface are more crucial.

The maximum circumferential stress values in and the von Mises maximum stress values were almost identical throughout all results. In order to use polar coordinates, the origin needs to be defined at the central point of the void. Otherwise, the stresses around the void will not be evaluated correctly. When there is more than one void, only the stress around one of the voids can be depicted correctly.

It is important to increase the element number significantly for good simulation results. When refining the mesh for the 2D-simulation both the smartsize meshing and mapped mesh showed convergence when the mesh was refined. In the case of smartsize meshing, the value without refinement is already close to convergence value. This is due to the fact, that with smartsize meshing the elements in the region around the void are rather small and dense. The region around the void is the critical area, because of the high stress gradients.

6 Outlook

The existence of pores inside parts manufactured by SLM leads to a great inconsistency regarding the mechanical properties. This is still a main issue and needs to be researched even further.

The simulation results were overall in excellent agreement with the theorical analytic formulas. Not only in regard to the maximum stresses but also the course of the stress around the void could be confirmed.

However, it is still difficult to make a direct comparison with the real-life behaviour of SLM parts. In the simulations many assumptions are made such as fully spherical holes, less amount of pores and no other defects compared to the real practical problems. In addition, in the FEM software many simplifications exist such as isotropy, smooth surfaces, ideal bearings and forces.

For a more exact analysis of a real-life SLM part, much more information is required. For instance, scans have to be made for finding out the exact shape, size, quantity and location of defects inside parts. Implementing this information into the FEM model will result in an extreme complex geometry, that will be nearly impossible to mesh. The time and costs would increase enormously. The accuracy of the simulation and computational effort conflict with each other.

Nevertheless, this work gives an important insight into FEM simulations of elliptical pores under tension. Many of the simulations could be confirmed.

7 Literature

[Braun et al., 2020]. Braun, M.; Müller, A. M., Milaković, A.-S.; Fricke, W.; Ehlers, S. (2020): Requirements for stress gradient-based fatigue assessment of notched structures according to theory of critical distance, Fatigue Fract Eng M, 43(7), pp. 1541-1554.

[Braun et al., 2020]. Braun, M.; Hellberg, S.; Kryukov, I.; Böhm, S.; Wu, R. E.; Ehlers, S.; Sheikhi, S. (2020. Untersuchung der Schwingfestigkeit hybrid additiv und subtraktiv gefertigter Proben aus AISI 316L, Proc. of 5. Tagung Additiv gefertigte Bauteile und Strukturen, Berlin, Germany, 4.–5.11.

[Bürgel, 2005]. Bürgel, Ralf (2005): Lehr- und Übungsbuch Festigkeitslehre. Mit 10 Tabellen; [mit 114 Aufgaben und 63 Seiten Lösungen. 1. Edition, Wiesbaden: Vieweg (Studium Technik, / Ralf Bürgel ; Bd. 1).

[Celik, 2020]. Celik, Emrah (2020): Additive manufacturing. Science and technology. 1. Edition, Berlin: Walter de Gruyter (De Gruyter graduate).

[Choren et al., 2013]. Choren, J. A.; Heinrich, S. M.; Silver-Thorn, M. B. (2013): Young’s modulus and volume porosity relationships for additive manufacturing applications. In J Mater Sci 48 (15), pp. 5103–5112. DOI: 10.1007/s10853-013-7237-5.

[Costes et al., 2006]. Costes, J. P.; Guillet, Y.; Poulachon, G.; Dessoly, M. (2006): Tool-life and wear mechanisms of CBN tools in machining of Inconel 718. In International Journal of Machine Tools and Manufacture 47 (7-8), pp. 1081–1087. DOI: 10.1016/j.ijmachtools.2006.09.031.

[Davis et al., 2017]. Davis, T.; Healy, D.; Bubeck, A.; Walker, R. (2017): Stress concentrations around voids in three dimensions: The roots of failure. In Journal of Structural Geology 102, pp. 193–207. DOI: 10.1016/j.jsg.2017.07.013.

[Dieter and Bacon, 1988]. Dieter, George Ellwood; Bacon, David (1988): Mechanical metallurgy. SI metric ed. London: McGraw-Hill (McGraw-Hill series in materials science and engineering).

[DIN EN ISO/ASTM 52900, 2018]. DIN German Institute for Standardization (2018): Additive manufacturing - General principles - Terminology (ISO/ASTM DIS 52900:2018); German and English version prEN ISO/ASTM 52900:2018. Berlin: Beuth Verlag.

[Fracturemechanics]. Fracture Mechanics. Stress Concentrations at Holes. URL: https://www.fracturemechanics.org/hole.html, Access date: 21.01.2021

[Garb et al., 2018]. Garb, Christian; Leitner, Martin; Tauscher, Markus; Weidt, Moritz; Brunner, Roland (2018): Statistical analysis of micropore size distributions in Al–Si castings evaluated by X-ray computed tomography. In International Journal of Materials Research 109 (10), pp. 889–899. DOI: 10.3139/146.111685.

[Griffiths et al., 2019]. Griffiths, Valeriya; Scanlan, James P.; Eres, Murat H.; Martinez-Sykora, Antonio; Chinchapatnam, Phani (2019): Cost-driven build orientation and bin packing of parts in Selective Laser Melting (SLM). In European Journal of Operational Research 273 (1), pp. 334–352. DOI: 10.1016/j.ejor.2018.07.053.

[Info-Palace]. Information Palace. Difference between Ductile and Brittle Materials with Stress Strain Curve. URL: https://www.informationpalace.com/difference-between-ductile-and-brittle-materials-with-stress-strain-curve/, Access: 21.01.2021.

[Heywood, 1952]. Heywood, R. B. (1952): Designing by Photoelasticity. London: Chapman & Hall Ltd.

[Kasperovich et al., 2016]. Kasperovich, Galina; Haubrich, Jan; Gussone, Joachim; Requena, Guillermo (2016): Correlation between porosity and processing parameters in TiAl6V4 produced by selective laser melting. In Materials & Design 105, pp. 160–170. DOI: 10.1016/j.matdes.2016.05.070.

[Khairallah et al., 2016]. Khairallah, Saad A.; Anderson, Andrew T.; Rubenchik, Alexander; King, Wayne E. (2016): Laser powder-bed fusion additive manufacturing: Physics of complex melt flow and formation mechanisms of pores, spatter, and denudation zones. In Acta Materialia 108, pp. 36–45. DOI: 10.1016/j.actamat.2016.02.014.

[Klocke, 2015]. Klocke, Fritz (2015): Gießen, Pulvermetallurgie, additive Manufacturing. 4. Edition. Düsseldorf: VDI-Verlag (VDI-Buch, / Wilfried König ; Bd. 5).

[Madenci and Guven, 2015]. Madenci, Erdogan; Guven, Ibrahim (2015): The Finite Element Method and Applications in Engineering Using ANSYS®. Boston, MA: Springer US.

[MAHER]. MAHER. Alloy 718 Data Sheet. URL: https://www.maher.com/media/pdfs/718-datasheet.pdf, Access date; 21.01.2021.

[Moussaoui et al., 2018]. Moussaoui, K.; Rubio, W.; Mousseigne, M.; Sultan, T.; Rezai, F. (2018): Effects of Selective Laser Melting additive manufacturing parameters of Inconel 718 on porosity, microstructure and mechanical properties. In Materials Science and Engineering: A 735, pp. 182–190. DOI: 10.1016/j.msea.2018.08.037.

[Peterson, 1965]. Peterson, R. E. (1965): The Interaction Effect of Neighboring Holes or Cavities, With Particular Reference to Pressure Vessels and Rocket Cases. In Journal of Basic Engineering 87 (4), pp. 879–884. DOI: 10.1115/1.3650834.

[W. Pilkey and D. Pilkey, 2008]. Pilkey, Walter D.; Pilkey, Deborah F.; Peterson, Rudolph Earl (2008): Peterson's stress concentration factors. 3rd ed. Hoboken N.J.: John Wiley.

[Prashanth, 2014]. Prashanth, K. (2014): Selective laser melting of Al-12Si. Doctoral dissertation, Technische Universität Dresden, Dresden. Faculty of Mechanical Science and Engineering.

[Schnabel et al., 2019]. Schnabel, Kai; Baumgartner, Jörg; Möller, Benjamin (2019): Consideration of defects in a fatigue assessment of additively manufactured metallic structures. In IIW Annual Assembly 2019 in Bratislava - Commission XIII (C-XIII) Document number: XIII-2796-19, DOI: 10.1016/j.prostr.2019.12.048.

[SLM-SOLU]. SLM Solutions. SLM 280 2.0. URL: https://www.slm-solutions.com/products-and-solutions/machines/slm-280-1/, Access date: 21.01.2021.

[M. Thompson and J. Thompson, 2017]. Thompson, Mary Kathryn; Thompson, John Martin (2017): ANSYS Mechanical APDL for Finite Element Analysis. San Diego: Elsevier Science. Available online at https://ebookcentral.proquest.com/lib/gbv/detail.action?docID=4931513.

[Tillmann et al., 2016]. Tillmann, W.; Schaak, C.; Nellesen, J.; Schaper, M.; Aydinöz, M. E.; Hoyer, K.-P. (2016): Hot isostatic pressing of IN718 components manufactured by selective laser melting. In Additive Manufacturing 13, pp. 93–102. DOI: 10.1016/j.addma.2016.11.006.

[Timoshenko, 1970]. Timoshenko, Stephen (1970): Theory of elasticity. Third edition. New Delhi, India: McGraw-Hill Education (Engineering societies monographs).

[Wohlers Associates]. Wohlers Associates. URL: https://wohlersassociates.com/press82.htm, Access date: 12.02.2021.

[Yadollahi and Shamsaei, 2017]. Yadollahi, Aref; Shamsaei, Nima (2017): Additive manufacturing of fatigue resistant materials: Challenges and opportunities. In International Journal of Fatigue 98, pp. 14–31. DOI: 10.1016/j.ijfatigue.2017.01.001.

8 Appendix

Following figures of results did not have enough additional significant meaning to the work and are therefore listed in the appendix:

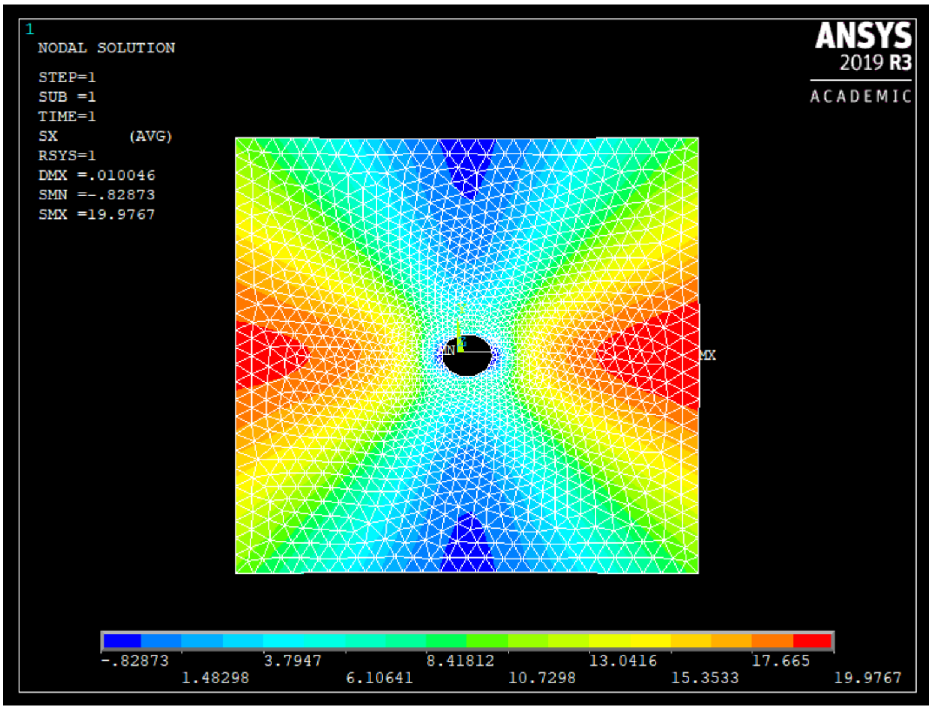

Figure 8-1: Radial stress distribution of 2D plane with a 5mm void

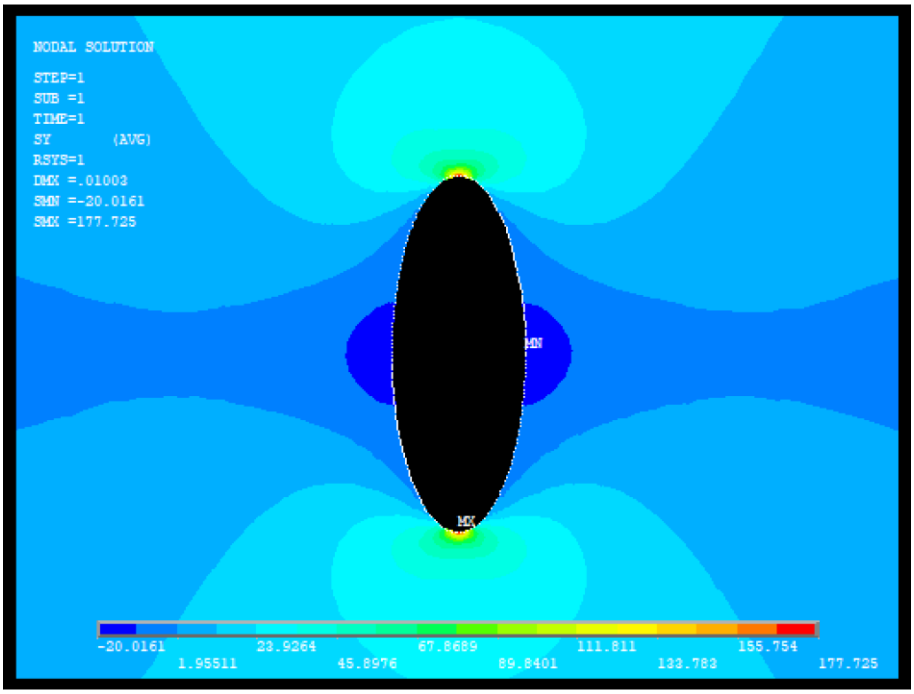

Figure 8-2: Circumferential stress distribution of 2D plane with an elliptical void [Zoom]

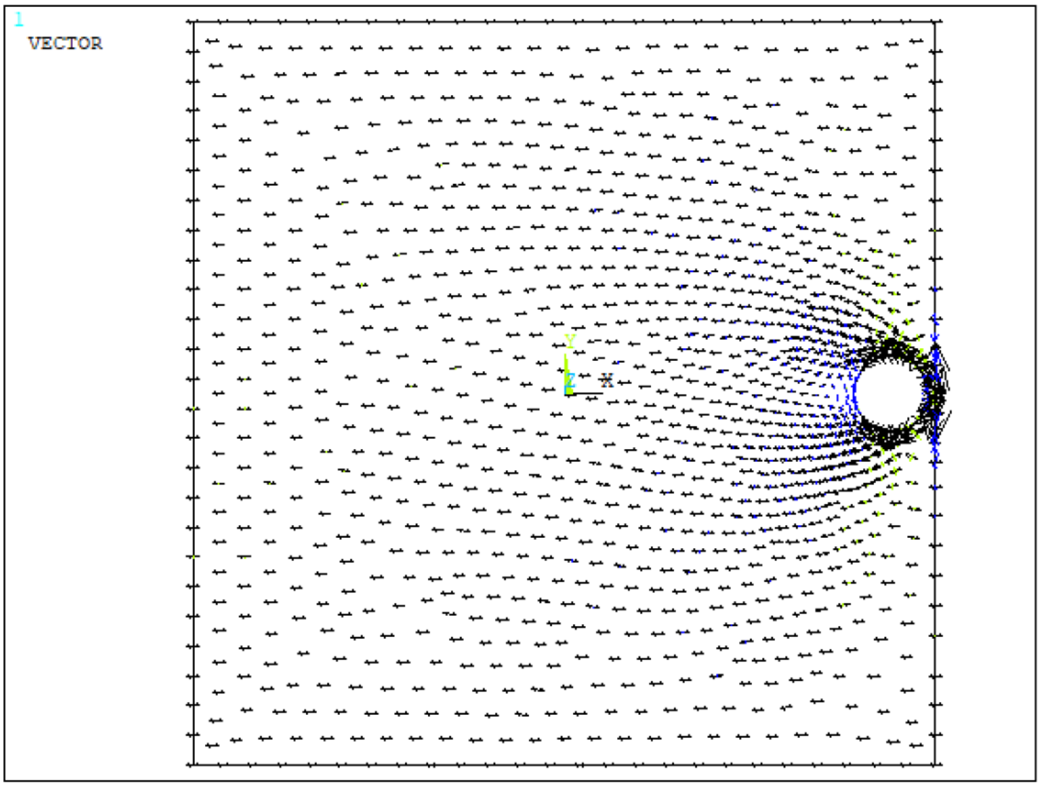

Figure 8-3: Vector plot of 2D plane with 5mm void near the loading side

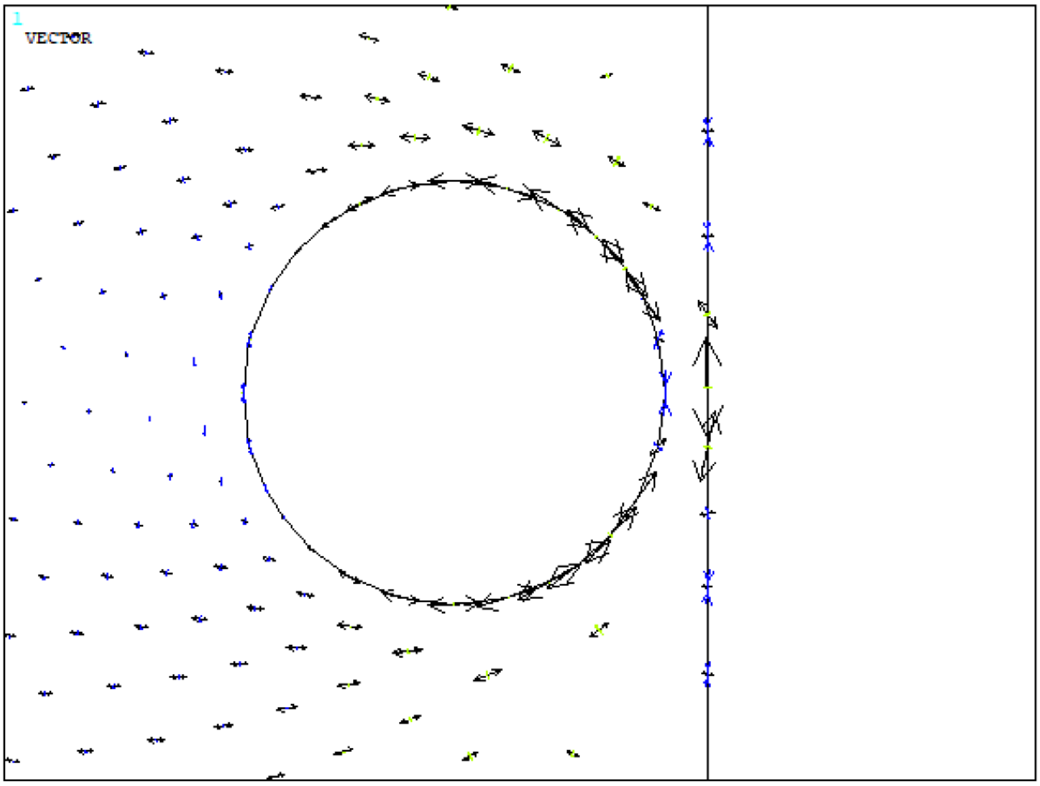

Figure 8-4: Vector plot of 2D plane with 5mm void near the loading side [zoom]

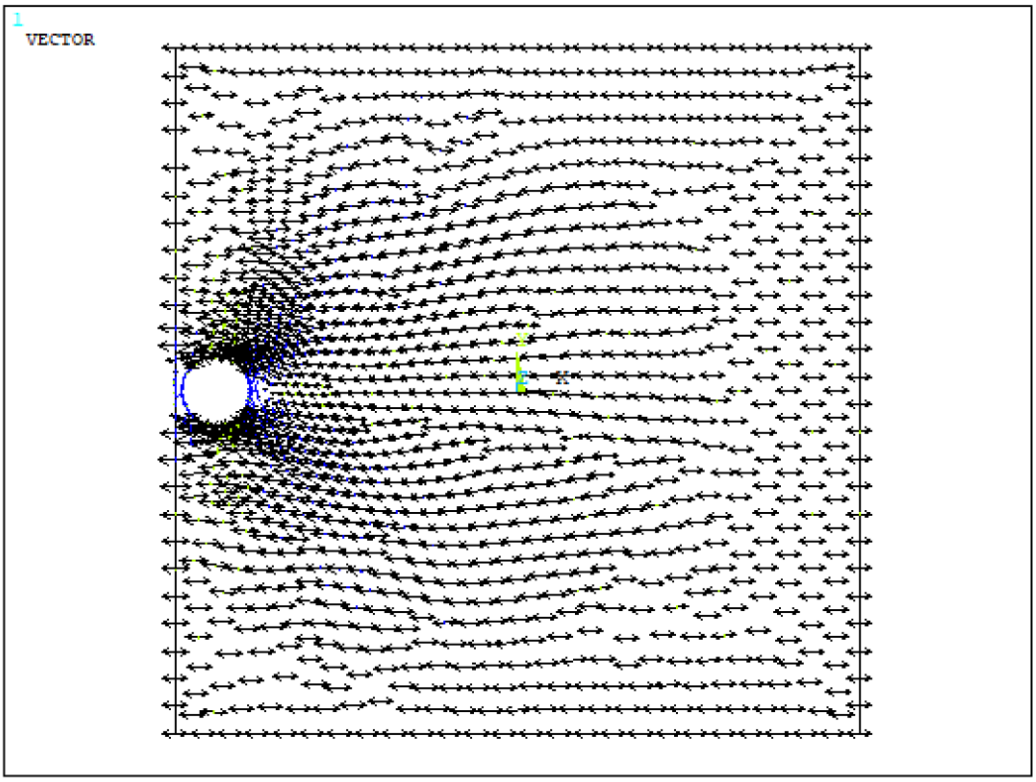

Figure 8-5: Vector plot of 2D plane with 5mm void near the bearing side

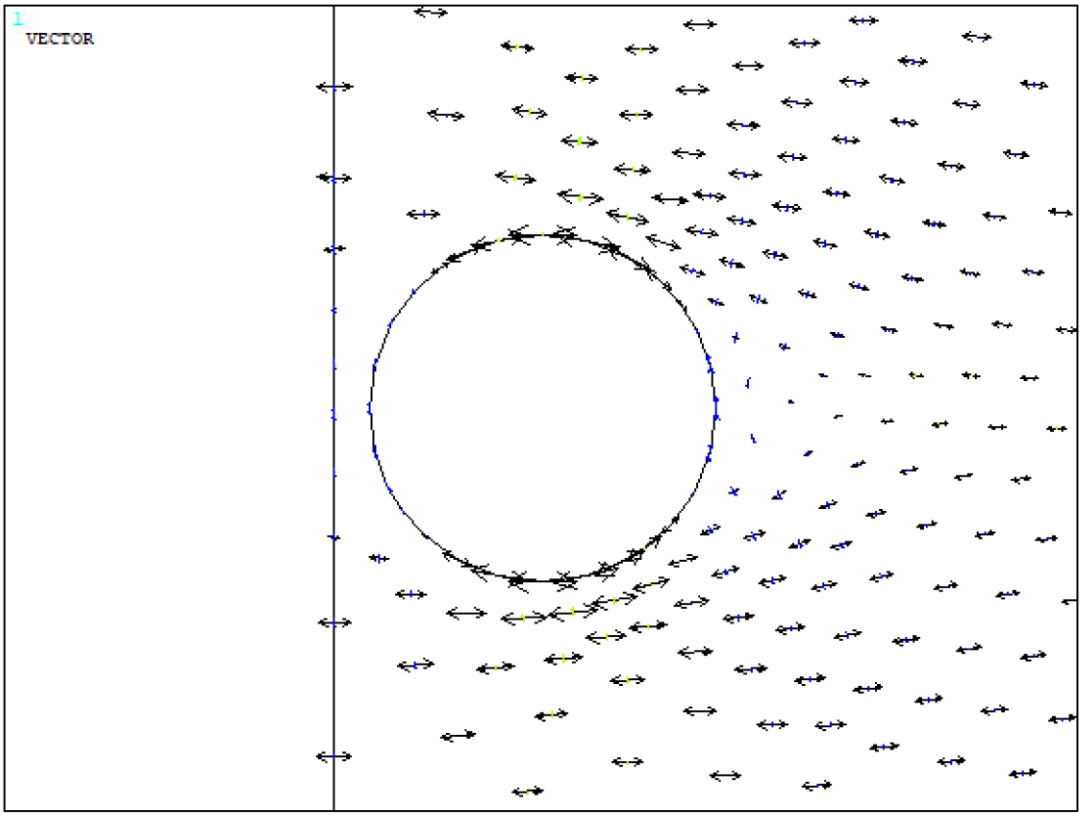

Figure 8-6: Vector plot of 2D plane with 5mm void near the bearing side [zoom]